Three-dimensional structure of a low-Reynolds-number turbulent boundary layer

By CARL J. DELO†, RICHARD M. KELSO‡
AND ALEXANDER J. SMITS

Department of Mechanical and Aerospace Engineering, Princeton University, Princeton,
New Jersey 08544-0710, USA

A low-Reynolds-number zero-pressure-gradient incompressible turbulent boundary layer was investigated using a volumetric imaging technique. The Reynolds number based on momentum thickness was 700. The flow was tagged with a passive scalar from two spanwise dye slots to distinguish between fluid motions originating in the inner and outer portions of the boundary layer. The resulting volumetric scalar field was interrogated using a laser sheet scanner developed for this study. Two- and three-dimensional time-dependent visualizations of a 50 volume time series are presented (equivalent to 17δ in length). In the outer portion of the boundary layer, scalar structures were observed to lie along lines in the (x, z)-plane, inclined to the streamwise (x-)direction in the range $\pm 50°$. The ejection of brightly dyed fluid packets from the near-wall region was observed to be spatially organized, and related to the passage of the large-scale scalar structures.

1. Introduction

Here, we present the short-term dynamics of a low-Reynolds-number turbulent boundary layer using three-dimensional visualizations of the scalar field. The interpretations are based on inspection of individual events in a data set comprising a 50 volume time series, equivalent to 17δ in length.

It is a well-established observation that a turbulent boundary layer displays structure, in that 'coherent motions' or 'organized motions' are recognized to be an important component of the velocity and pressure fields. Such coherent structures were described by Robinson (1991) as 'a three-dimensional region of the flow over which at least one fundamental flow variable (velocity component, density, temperature, etc.) exhibits significant correlation with itself or with another flow variable over a range of space and/or time that is significantly larger than the smallest local scales of the flow.'

Different features appear in the near-wall and outer-layer regions, and we have a broad understanding of their general features. In contrast, the fundamental nature of the motions, their distinguishing characteristics, and the nature of their interactions, are not at all settled. According to an early review by Cantwell (1981), the structure

---

† Present address: NASA Goddard Institute for Space Studies, Columbia University, New York, New York, 10025.

‡ Present address: Department of Mechanical Engineering, University of Adelaide, South Australia 5005, Australia.

in the near-wall region consists of a fluctuating array of streamwise counter-rotating vortices, where the vortices densely cover all parts of the wall. Just above the streamwise vortices, but still quite close to the wall, is a layer that is regularly battered by bursts that involve very intense small-scale motions of energetic fluid ('energetic near-wall eddies'). The outer layer is also occupied by intense small-scale motions ('energetic outer-flow eddies'). These are found primarily on the upstream-facing portions of the turbulent/non-turbulent interface, that is, the backs of the 'bulges' in the outer part of the layer. The outer small-scale motions are part of an overall transverse rotation, sometimes called the large-scale motions (LSM). The LSM have a scale comparable to the thickness of the layer.

A significant body of evidence supports the existence of hairpin or lambda vortices in the turbulent boundary layer (see Robinson (1991) for a review, and other papers discussed below). The range of scales of motions, including the LSM and small-scale motions, and much of the statistical behaviour of the turbulent boundary layer, are explained by the existence of a heirarchy of scales of such vortices within the layer.

Cantwell states the commonly held view that the low-speed streaks are experimentally observable evidence of pairs of streamwise-oriented counter-rotating vortices in the near-wall region (see e.g. Blackwelder & Kaplan 1976; Blackwelder 1978; Praturi & Brodkey 1978; Smith & Schwartz 1983). Smith *et al.* (1991) make convincing arguments that the low-speed streaks are, in fact, artefacts of the passage of symmetric and asymmetric hairpin vortices. These two views can be reconciled by the assumption that the streamwise vortices in the near-wall region are the trailing 'legs' of 'hairpin' or 'lambda-shaped' or 'horseshoe' vortices that are attached to the wall. Visual evidence of this aspect of hairpin vortex structure is lacking. It is an open question whether this lack is due to the extreme stretching that the legs undergo, and a consequent difficulty in their visual detection, or whether the counter-rotating vortices are, in fact, not directly connected to the horseshoes. The existence of the streaks is, however, well established (see e.g. Kline *et al.* 1967; Kim, Kline & Reynolds 1971; Eckelmann 1974). Note that the difference between horseshoe, hairpin and lambda vortices is largely a function of Reynolds number (Head & Banyopadhyay 1981), with low-Reynolds-number structures having a more horseshoe-like appearance.

The spanwise spacing of the streaks is one of the few universally accepted aspects of boundary-layer structure, where $\lambda^+ \approx 100$ (here $\lambda^+ = \lambda u_\tau / \nu$, λ is the spanwise wavelength, u_τ is the friction velocity given by $\sqrt{\tau_w/\rho}$, ν is the fluid kinematic viscosity, ρ is its density, and τ_w is the wall shear stress). In contrast, estimates of the streamwise extent of the streaks varies widely. This is most probably due to the different methods used to make the estimates. The low-speed streaks are seen to extend up to $L_x^+ \approx 2000$ in some cases, if the spanwise meandering of the streaks is taken into account. Velocity correlation methods derived from stationary probes would tend to underestimate the streamwise length of a meandering streamwise vortex, as only limited portions of such a meandering vortex would intersect the probe. In addition, as Cantwell points out, even if the low-speed streaks are generated directly by pairs of counter-rotating vortices, it does not necessarily follow that the two must have the same streamwise dimension (see also Smith *et al.* 1991). The persistence distance of the near-wall vortices is difficult to evaluate for the same reasons.

The convection velocities of the various types of structure are also fairly well established, and the values represent data from a wide range of studies, primarily correlation-based. The convection velocity of the near-wall streamwise vortices is probably close to the local mean velocity, as Cantwell reports that the low- and high-speed streaks move at about 50% and 150% of the local mean velocity, respectively.

In contrast to the general agreement on the kinematics of the structures, the mean spatial organization of the structures is for the most part undetermined. The mean streamwise and spanwise separations of the LSM reported by various authors exhibit significant variations, and there is no indication of an observed spanwise angular orientation. Information on the mean spatial separation of the small-scale eddies is also lacking.

Generally, the investigation of the large-eddy structure in boundary layers through the use of correlation techniques suffers from some serious drawbacks. Correlation analyses of ensemble-averaged data necessarily disregard the instantaneous global organization of the flow field. As a given portion of a turbulent flow is composed of structures of varying age and levels of activity, ensemble-averaged approaches may present a more complicated or confused picture of the flow than actually exists.

Liu, Adrian & Hanratty (2001), Adrian, Meinhart & Tomkins (2000) and Zhou *et al.* (1999) have provided insight on the generation of coherent hairpin vortex packets containing a multiplicity of spatially organized hairpin-like vortices in channel and boundary-layer flows. The earlier observations by Bandyopadhyay (1980) and Head & Banyopadhyay (1981) on these packets with a characteristic upstream interface, sloping at about 12° to 20°, were confirmed using numerical simulations and PIV experiments. An elegant conceptual model of nested packets of hairpins (or fragments thereof) growing from the wall was developed. This model is illustrated in figure 25 of Adrian *et al.* (2000). The resulting hierarchy of motions, with changes of scale as a result of vortex pairing, is in the same spirit as the mechanism of wall turbulence proposed by Perry & Chong (1982). Strong confirmation of the statistical significance of coherent hairpin packets has been provided by Marusic (2001) and Christensen & Adrian (2001). Of particular relevance to the present project is the observation by Adrian *et al.* (2000) that at low-Reynolds-number, such packets contain 2–3 vortices, and that the number of vortices and the range of scales present increases with increasing Reynolds numbers.

Praturi & Brodkey (1978) recognized the need to study the three-dimensional structure of the turbulent boundary layer in order to understand its mechanisms. Their experiments, using stereoscopic visualization of suspended particles, provided the first detailed insights into the three-dimensional flow structure. The present paper uses a new three-dimensional technique to obtain an improved data set that allows both qualitative and quantitative analysis. In particular, the data reveal the meandering motions of the near-wall streaks and the multiple ejections observed above the streaks, and details of the temporal and spatial organization of the coherent structures in the boundary layer.

The possibility of detecting spatial arrangements of structures in the boundary layer to provide evidence of large-scale organization and/or interaction has influenced the design of the experiment carried out here. The flow volume examined was chosen to give a large field of view in the spanwise and streamwise directions in order to detect complete, inclined horseshoe vortices. The arrangement was chosen to establish (if possible) the general physical characteristics of the horseshoe vortices and their spatial relationship with each other, and with the near-wall streaks found in the boundary layer.

The highly complex nature of the three-dimensional time-evolving velocity and vorticity fields suggested the use of volumetric imaging of a passive scalar to reveal the spatial and temporal characteristics of the large-scale structure. As recognized by Brown & Thomas (1977) and Praturi & Brodkey (1978) (among others), the essentially three-dimensional character of boundary-layer motions makes it very difficult to detect a complex process, such as the bursting cycle, unambiguously from a fixed
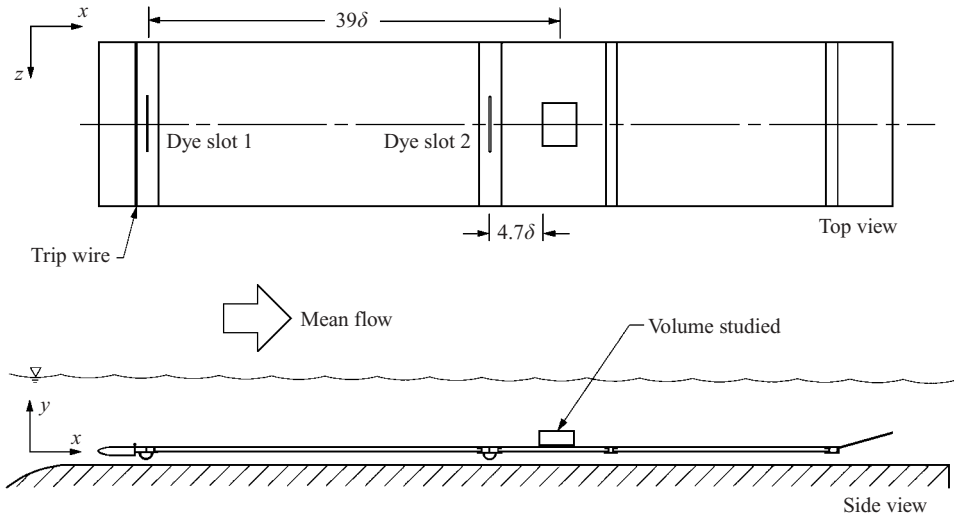
FIGURE 1. Experimental configuration.

measurement station. Part of the problem is no doubt because more than one fluid packet may be ejected from a given low-speed streak, so the identification of a single bursting event becomes ambiguous (Luchik & Tiederman 1987). Additionally, the different detection methods employed add to the confusion (e.g. visual identification, quadrant analysis, conditional sampling, see Bogard & Tiederman 1986). In this respect, visual studies have an advantage since an overall view of the flow field may be used to judge what part of a turbulent motion is to be investigated in a given realization. Extending this concept, it is logical to assume that a complete three-dimensional visualization of the flow field is more appropriate for revealing the complex spatial interrelationships in the boundary layer. A full volumetric view may be subsampled into standard two-dimensional renderings, but knowledge of the entire volume may be necessary in order for the two-dimensional sampling to effectively reveal the important dynamics.

To this end, a time series of 1600 consecutive volumes of boundary-layer data was collected. The volumes were collected in the form of image stacks; each volume was composed of 20 x–z images of scalar intensity, uniformly separated in the y-direction. The coordinate system is defined in figure 1. Initially, stereoscopic renderings of a 50-volume subset of the complete time series were generated in order to gain an overall picture of the structures present and to guide subsequent analysis.

Preliminary evidence of ejection events beneath large-scale structures in the stereoscopic views led to resampling the data set in various two-dimensional planes. The x–y time series was extracted from the volumetric data at 20 spanwise locations, and these indicated that ejection events were indeed occurring. The use of the two interrogation methods to examine the structure and dynamics of the boundary layer was an iterative process. For example, if a stereoscopic visualization suggested the occurrence of an ejection-type event, the given volume was resliced in various planes to investigate the time-dependent behaviour of the near-wall fluid and its spatial relationship to the neighbouring outer-layer structure. There was frequent reference back to the original x–z data slices to confirm any inferences drawn.

The data presented in this paper pertain to a tripped turbulent boundary layer with a Reynolds number of 700, based on momentum thickness. At such a Reynolds

number, we expect there to exist a small range of eddy scales in the boundary layer (Head & Banyopadhyay 1981). Nevertheless, we expect many of the findings from this study to be applicable to higher-Reynolds-number turbulent boundary layers in general.

In the present paper the term 'packet' is used to describe regions of brightly marked dye within the boundary layer. This should not be confused with the use of the word 'packet' in other recent publications to describe coherent groups of hairpin vortices. The use of packet in the present paper is chosen to maintain consistency with the terminology used in Delo & Smits (1997).

2. Experiment

Experiments were conducted in a closed-loop free-surface water channel with a full-width flat plate positioned in the test section, as shown in figure 1. An elliptical leading edge with a major : minor axis ratio of 4:1 was connected to a section containing the first dye injection port. A 2.38 mm trip wire was located at the junction of the elliptical leading edge and the dye port section. Each dye slot was 150 mm long in the spanwise direction, centred on the channel span, with a width (in the streamwise direction) of 0.51 mm. The first dye slot was located 32 mm downstream of the trip wire, and the second dye slot was located 958 mm downstream of the trip wire, just upstream of the flow region that was studied. Further details of the experiment are given by Delo (1996).

The boundary-layer mean flow properties were determined using a hydrogen bubble correlation technique similar to that used by Lu & Smith (1985) (see Delo 1996; Delo & Smits 1997). The free-stream velocity was $U_e = 230$ mm s^{-1} and the boundary-layer thickness at the upstream edge of the volume was $\delta = 27$ mm. The Reynolds number based on momentum thickness was $Re_\theta = \theta U_e / \nu = 700$, the friction velocity, $u_\tau = 11$ mm s^{-1}, and the von Kármán number $\delta^+ = \delta u_\tau / \nu = 300$.

Flow visualizations were obtained using disodium fluorescein dye illuminated with an argon ion laser sheet. The sheet was rapidly scanned through the flow by a laser sheet scanning apparatus, as shown in figures 2. The laser sheets were imaged with a high-speed analogue video system, then digitized and reassembled into volumes for subsequent visualization and quantitative analysis.

The two-point flow-tagging scheme developed by Goldstein (1991) was used in order to distinguish between fluid in the inner and outer portions of the boundary layer. The upstream dye slot, situated just behind the trip wire, was used to give a discernible background dye level to the turbulent fluid throughout the boundary layer. The dye was heavily concentrated (500 p.p.m. by weight) to offset the effects of turbulent diffusion and the entrainment of undyed free-stream fluid. The downstream dye slot was placed just upstream of the interrogation volume in order to brightly mark near-wall fluid. Because of the close proximity of the second slot, the dye released was less concentrated (250 p.p.m.), while still being distinguishably brighter than the dye marking the outer-layer fluid. The scalar released from the first dye slot was assumed to give a good indication of the large-scale structure in the boundary layer, particularly the turbulent–non-turbulent interface, and the scalar released from the second dye slot was tracked in order to investigate near-wall motions. The two dye slots were located 39δ and 4.7δ, respectively, upstream of the leading edge of the volume. See Goldstein & Smits (1994) and Delo (1996) for a discussion of Schmidt-number effects on the two-point flow-tagging scheme. The high concentration of dye
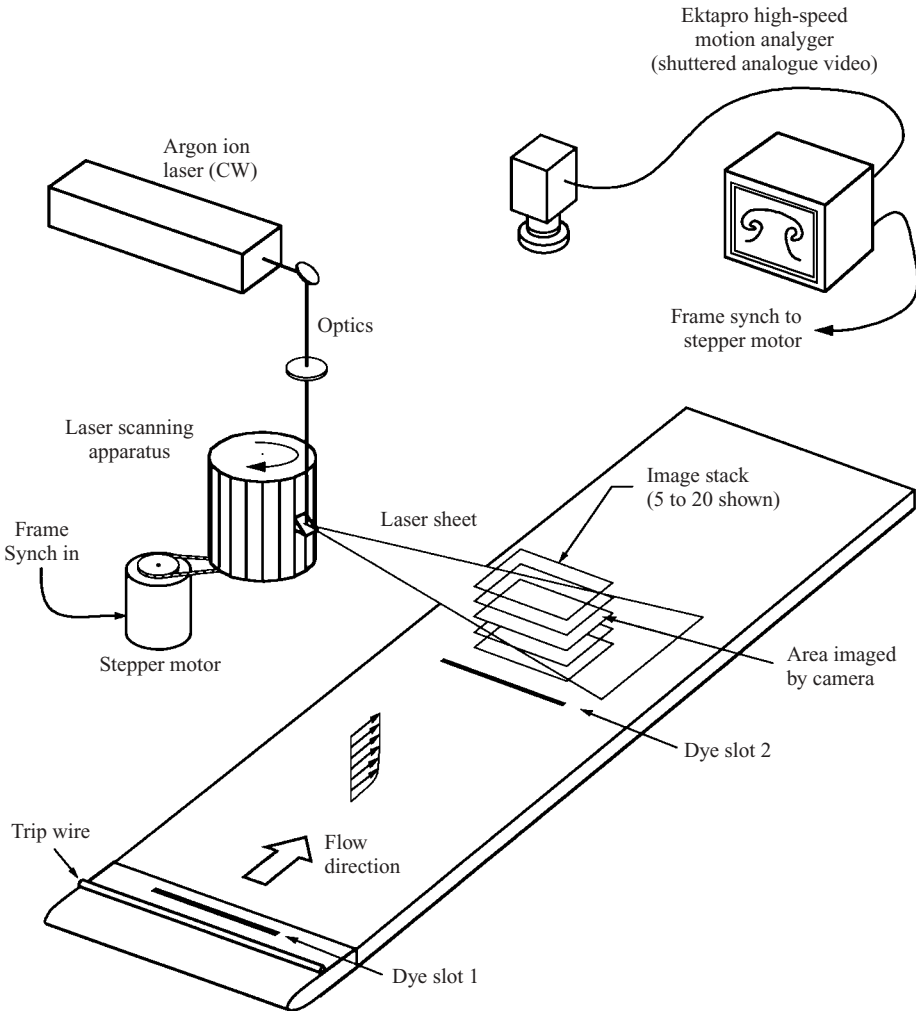
FIGURE 2. Experimental arrangement for the volumetric laser scanning.

led to some attenuation of the laser light, particularly in the near-wall region. The high concentration overall was necessary because of the low sensitivity of the imager and limitation in the strength of the laser source.

The laser sheet scanning apparatus shown in figure 2 forms a stack of 20 laser sheets by sweeping a focused laser beam through the flow volume parallel to the flat plate (in x–z planes) at 20 y-locations. To sweep the beam, a helical array of $45°$ mirrors was fixed to 20 faceted faces of a rotating drum. The focused beam of a 5 W CW argon ion laser (operating in single line mode, 501 nm, 1.8 W nominal power) was directed parallel to the axis of the drum, and reflected off each mirror as the drum rotated. The rotation of the flat mirror face caused the reflected beam to sweep through an angle of $18°$. The resulting laser sheet had uniform intensity, and its y-location (determined by the position of the mirror on the drum) was precisely repeatable. As the drum continued to turn, the beam reflected off the next mirror in the helix, forming another sheet at a different y-location. For this experiment, the bottom x–z laser sheet was at $y = 2$ mm, with uniform 2 mm separation in the

y-direction ($\Delta y/\delta = 0.074$, $\Delta y^+ = 22$). The useful portion of the interrogation volume measured: $L_x/\delta = 3.5$, $L_y/\delta = 1.5$, $L_z/\delta = 3.3$ (in viscous units: $L_x^+ = 1050$, $L_y^+ = 440$, $L_z^+ = 1000$). For a detailed discussion of the laser scanning system, see Delo & Smits (1993, 1997), Delo, Poggie & Smits (1994) and Delo (1996).

The scanner was driven by a stepper motor synchronized to the frame-rate signal from the analogue video imager. The laser sheets were imaged from directly overhead with a Kodak/Spin Physics Ektapro 1000 High-speed Motion Analyser. Images were acquired at 500 frame s^{-1}, yielding 25 full volumes per second. The rotation of the drum was such that the top slice of each volume was imaged first, the next lower slice 0.002 s later, and so on. By comparison, the outer time scale or 'eddy turnover time' is $t_\delta = \delta/U_e = 0.117$ s, whereas the inner time scale is $t^+ = \nu/u_\tau^2 = 0.00812$. The elapsed time between subsequent volumes ($\Delta t = 0.04$ s) corresponded to approximately one third of a characteristic 'eddy turnover time' ($\Delta t U_e/\delta = 0.34$; $\Delta t u_\tau^2/\nu = 4.9$). The time resolution was therefore adequate for the examination of large-scale coherent structures, and no interpolation in time was performed. Initially, one thousand sequential images of the data set were digitized and stored as computer files. These images constitute 50 volumes (time steps 1–50), covering an elapsed time of $\Delta T = 2.00$ s ($\Delta T U_e/\delta = 17.0$; $\Delta T u_\tau^2/\nu = 250$). Additional volumes (every tenth volume from time steps 51–1611) from the complete data set have been digitized, but will not be presented here. The full data set spanned an elapsed time of 65 s ($\Delta T U_e/\delta = 550$; $\Delta T u_\tau^2/\nu = 7900$).

The component images of the stacks were digitized with 8-bit resolution using an Imaging Technologies Series 151 frame grabber controlled with Whyndham–Hannaway image processing software. The pixel resolution was 0.25 mm (0.0093δ; $2.78\nu/u_\tau$). After preliminary image processing to remove noise, a correction was made to account for convection during image stack acquisition. The slices were offset in the x-direction based on the mean convection velocity of the scalar field at each laser sheet height and the time delay during stack acquisition. The correction was performed to preserve the spatial orientation of the structures in the visualizations, particularly their inclination in the (x, y)-plane. For further details, see Delo (1996) and Delo & Smits (1997).

The paired projections of the volumetric data used to create the stereoscopic visualizations were calculated with a volume rendering program developed by Delo *et al.* (1994). The program generates true translucent volumetric views of an image stack using a ray-tracing method, using a source-attenuation model (Beer's law) to create a pair of monochrome projections of a stack of two-dimensional images. The projections from the two viewpoints were calculated separately, then combined to form the anaglyph (two-colour) stereograms. These were used extensively for stereoscopic viewing of data sets during analysis. Stereopairs were also readily generated by placing the left and right greyscale images side-by-side on the page. The stereopairs may be viewed with a stereoscope of binocular design (i.e. lenses to direct each image to the appropriate eye). If no such viewer is available, the merging of the two views may be achieved by relaxing the eyes (for example, by focusing on a distant object) until the direction of view of the two eyes is parallel, then moving the stereopair into the field of view. This may require practice. Examples of such images are presented in figure 6. For further information, see Delo & Smits (1997).

The stereoscopic time series was calculated with overhead and oblique viewpoints as indicated in figure 3. The first was from a viewpoint directly overhead, looking down on the volumes in the negative y-direction. In this view, the flow is from bottom to top, parallel to the viewing plane. The second time series was from an oblique
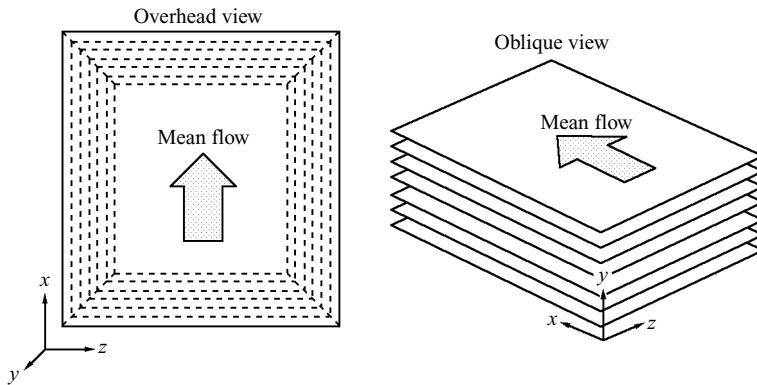
FIGURE 3. Viewpoints used for the generation of stereoscopic time series.

viewpoint. For the stereoscopic renderings, a grid has been added to the image stacks to represent the surface of the flat plate in order to orient the viewer, to give a spatial reference for the location of structures, and to impart a sense of scale (grid spacing 0.5δ).

MPEG movies of the stereoscopic time series are presented in Delo & Smits (1997) for the processed x–z data slices at $y/\delta = 0.37$, 0.74 and 1.12 ($y^+ = 111, 222, 333$). They are available on the web (http://elecpress.monash.edu.au/ijfd/1997_vol1/ paper3/DeloSmits.html). When viewing these movies, note particularly the diagonal organization of the large-scale outer-layer structure evident in the overhead view. These diagonal arrays of structures are generally accompanied by coordinated ejections of near-wall fluid from locations distributed spanwise beneath the outer-layer structure. Early indications of strong global spatial organization of the coherent structures in the boundary layer led to the extension of the original data set from 50 to 151 volumes. This extended data set will be examined first to give a qualitative overview of the structures that were found in the boundary layer. Large-scale structures in the 50 volume data set will then be examined in more detail, as well as their relation to inner-layer-structure.

3. Overview of the full data set

To give a physical representation of the extended data set, composite images were formed at each of the 20 y-levels that incorporate the data slices from time steps 1, 11, 21 and so on through time step 151. These composite images essentially depict a time series of images at each level. Composite images at three levels ($y/\delta = 1.12$, 0.743 and 0.372) are presented for time steps 101–151 in figure 4. Here, the top image is from time step 101, the next image is from time step 111, shifted vertically on the page by 3.4δ, and so on for every tenth image in the data set at that level, ending with time step 151. The offset of 3.4δ represents the distance travelled by the free-stream flow during 10 time steps, that is, $\Delta x = U_e \Delta t$. The result is a large-scale image, which gives a scaled spatial approximation of a time-dependent data set. Each composite image measures 20.5δ by 3.34δ in the x- and z-directions, respectively.

The images in the composites at lower levels in the boundary layer were assembled using the displacement calculated using the free-stream velocity, rather than the local mean velocity. This was done to maintain the relative physical positions of the slices within the component volumes, hence preserving the spatial relationship
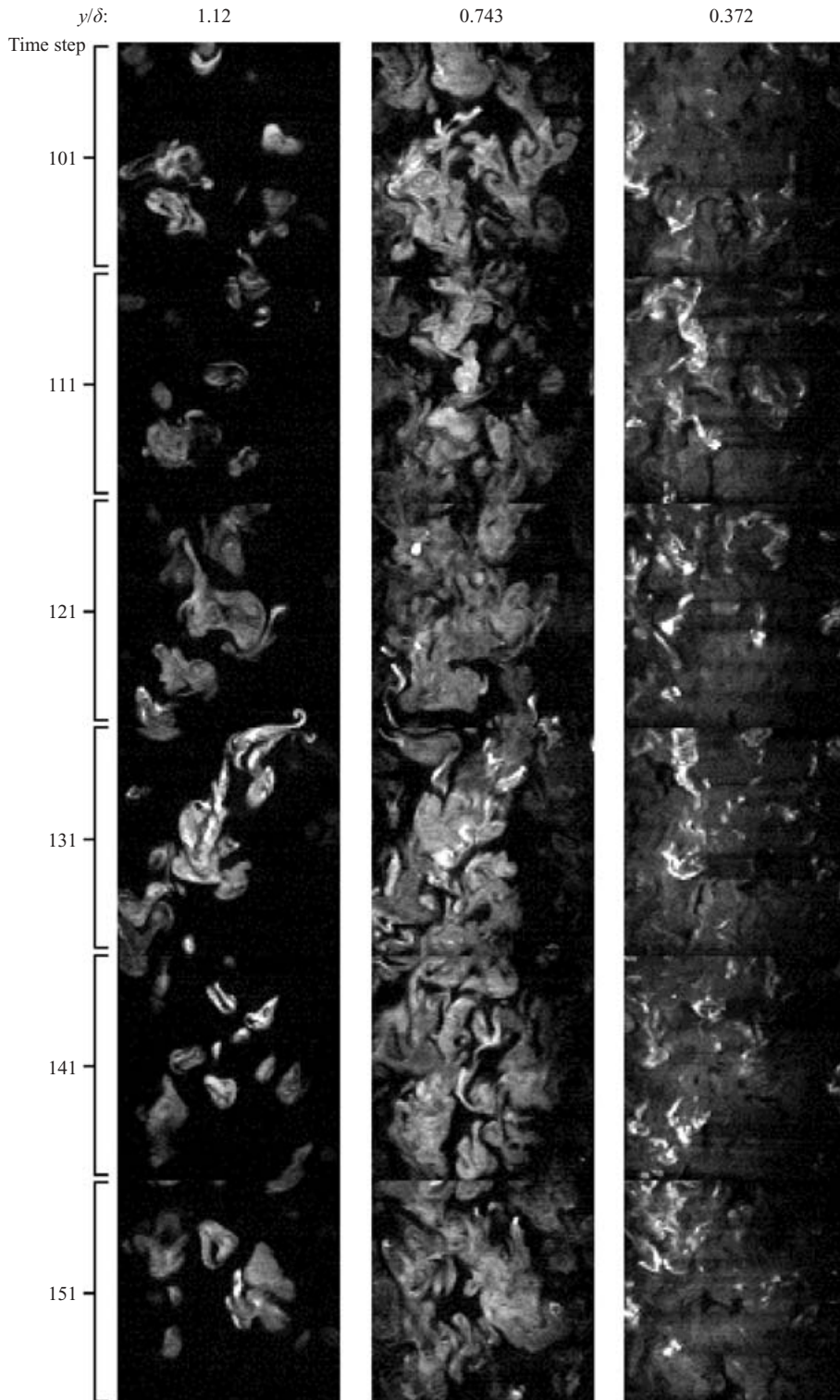
FIGURE 4. Composite x–z images of time steps 101–151 at three heights in the boundary layer. The 'flow' direction is from bottom to top. Each image measures $L_z/\delta = 3.34$ by $L_x/\delta = 20.5$.
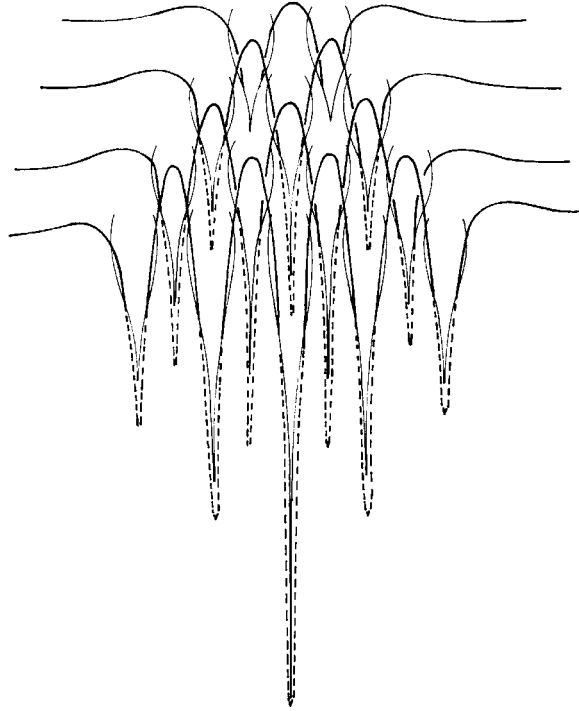
FIGURE 5. Diagram of the sequence of events leading to the formation of a turbulent spot in terms of vortex filaments. [After Perry, Lim & Teh 1981].

between inner- and outer-layer structures. It is worth noting that because of the low convection velocities near the wall, a brightly dyed near-wall streak may appear in two subsequent volumes at different stages in its evolution. This is not a serious drawback in the context of a qualitative overview of the data set.

As mentioned in §2, the use of a high dye concentration from the downstream slot led to some attenuation of the laser light, particularly near the wall. In each composite image, the laser entered the flow from the left-hand side, so the attenuation is evident on the right-hand side. This effect is only significant in the slices adjacent to the floor, and is insignificant in the outer layers.

The global organization of the boundary-layer structure is evident in the composite images, particularly in the outer layer at $y/\delta = 1.12$. The large-scale structures in the outer layer are occasionally arrayed along diagonal lines, inclined to the stream-wise direction within the range of (approximately) $-45°$ to $+45°$. Quantitative evidence of this is presented in §4. This linear orientation is especially apparent in time steps 31–41, 61–91 and 121–141, and is strongly reminiscent of the orientation of vortex filaments in a turbulent spot proposed by Perry, Lim & Teh (1981), although the orientation is not as symmetric as it is in their proposed model. The model of Perry *et al.* is shown in figure 5. Such a very large-scale spatial organization has not been remarked upon by most workers, though evidence of it may be found in a number of visually based experimental studies (see for example the visualizations in Smith & Smits 1995).

Inspection of the composite images at $y/\delta = 0.743$ shows that this diagonal inclination continues at lower levels, though the higher level of complexity masks it to some extent. This is to be expected, given the presumption that outer-layer

structures extend into the near-wall region. In the near-wall region, no strong diagonal orientation is immediately apparent. The brightly dyed streaks in the near-wall region, however, do appear to be associated (though not exclusively) with the very large-scale agglomerations. This is an important point that will be investigated further in §4.

The composite images of the extended data set were then assembled into image stacks. Stereoscopic renderings of the full data set from an overhead viewpoint are presented in figure 6. To view these as stereopairs, the page must be rotated 90° clockwise, so that the 'flow' is from left to right. A 1δ square floor grid has been added to the stacks for reference.

The overhead view in figure 6 demonstrates the wide range of structure size and shape found in the outer region of the boundary layer. The diagonal organization of the large-scale structures, noted in the composite images, is particularly apparent; the volume-visualization technique reduces the complexity of the individual data slices by providing a volumetric synthesis of the smaller scalar elements into a connected picture of the large-scale scalar structures. This results in a clearer picture of the connectedness of the scalar structures, and the spatial relationships among them.

Note the very large scale quasi-streamwise agglomerations of structures which occur in all three segments of the visualizations. These agglomerations can be very large, sometimes extending up to 4 or 5δ in streamwise extent. The agglomerations are generally inclined to the free stream within the same angular range as the diagonal lines along which structures appear to be spaced at approximately $\pm45°$ to the free-stream direction. They are approximately 1δ wide, and sometimes stretch across 3δ in the spanwise direction. These structures are similar in geometry to the 'bulges' described in §1, and are presumably the scalar signature of the large-scale motions (LSM). Although the agglomerations are sometimes much more extensive in the streamwise direction than would be expected (1–3δ streamwise length), the occasionally large skew angle of the structures would result in a lower estimate of their length if the structure was sampled only in the (x, y)-plane. The similar orientation of the large-scale agglomerations and the diagonal spacing of smaller-scale distinct structures, may provide clues to the formation of the LSM.

Note that the large agglomerations are generally surrounded by undyed fluid in the outer part of the boundary layer, with regions of undyed fluid extending to the wall on one or both sides of the structure. The deep incursion of undyed fluid suggests that these large structures may be responsible for significant entrainment of free-stream fluid into the near-wall region. It may suggest that the presence of these large structures inhibits the generation of new scalar structures in their immediate vicinity.

Figure 7 shows resampled images from the composite stacks at two spanwise locations ($z/\delta = 0.75$ and 1.42; $z^+ = 225$ and 425). To view these images, the page must be rotated 90° clockwise, so that the 'flow' is from left to right. These images show the predominant downstream-leaning inclination of the individual structures, and confirm the highly complex nature of the boundary layer. It is evident from the figure that bright streaks of dyed fluid often appear directly beneath cross-sections of large-scale outer-layer structures, although not exclusively. Several of the streaks exhibit a sinuous cross-section, suggestive of a low-speed streak undergoing unstable oscillations during the process of lifting away from the wall.

There is also evidence in figure 7 that large packets of concentrated near-wall fluid have migrated well into the outer part of the boundary layer. The movement of
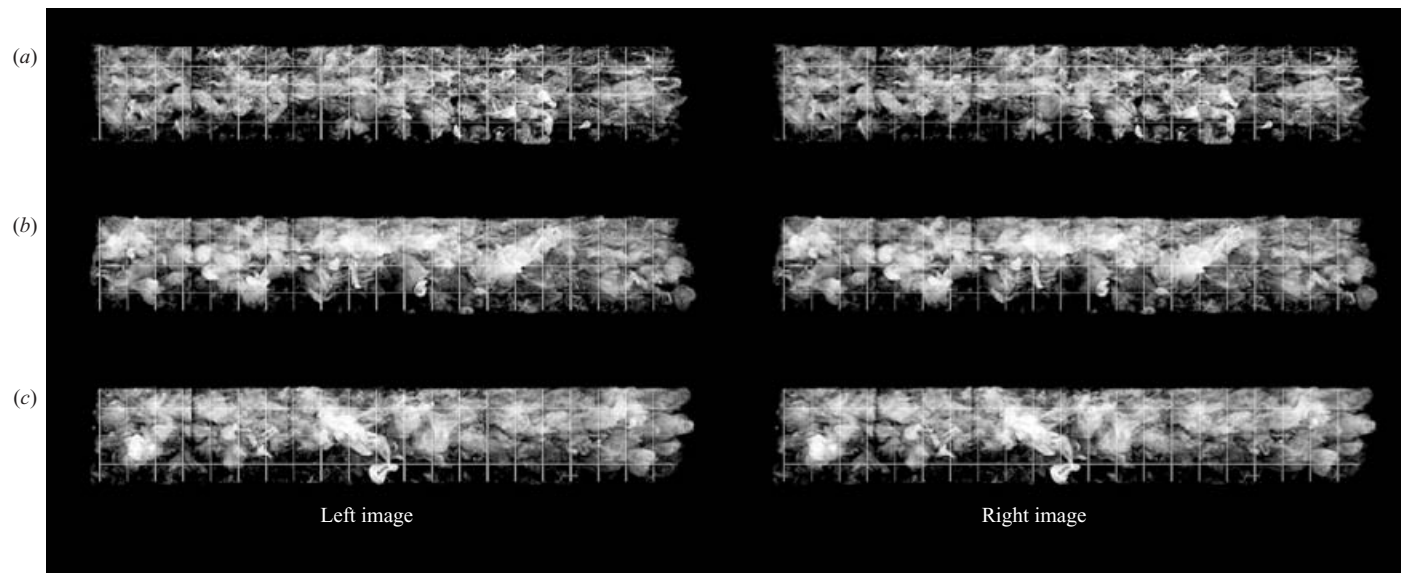
Left image   Right image

FIGURE 6. Stereoscopic visualization of the composite data set, top view. The stereopair can be reconstructed using a stereoscopic viewer. 'Flow' is from left to right, and the grid spacing is 1δ. (a) Timesteps 1–51, (b) timesteps 51–101 and (c) timesteps 101–151. Each of the three segments of the full data set measures $L_z/\delta = 3.34$ by $L_x/\delta = 20.5$.
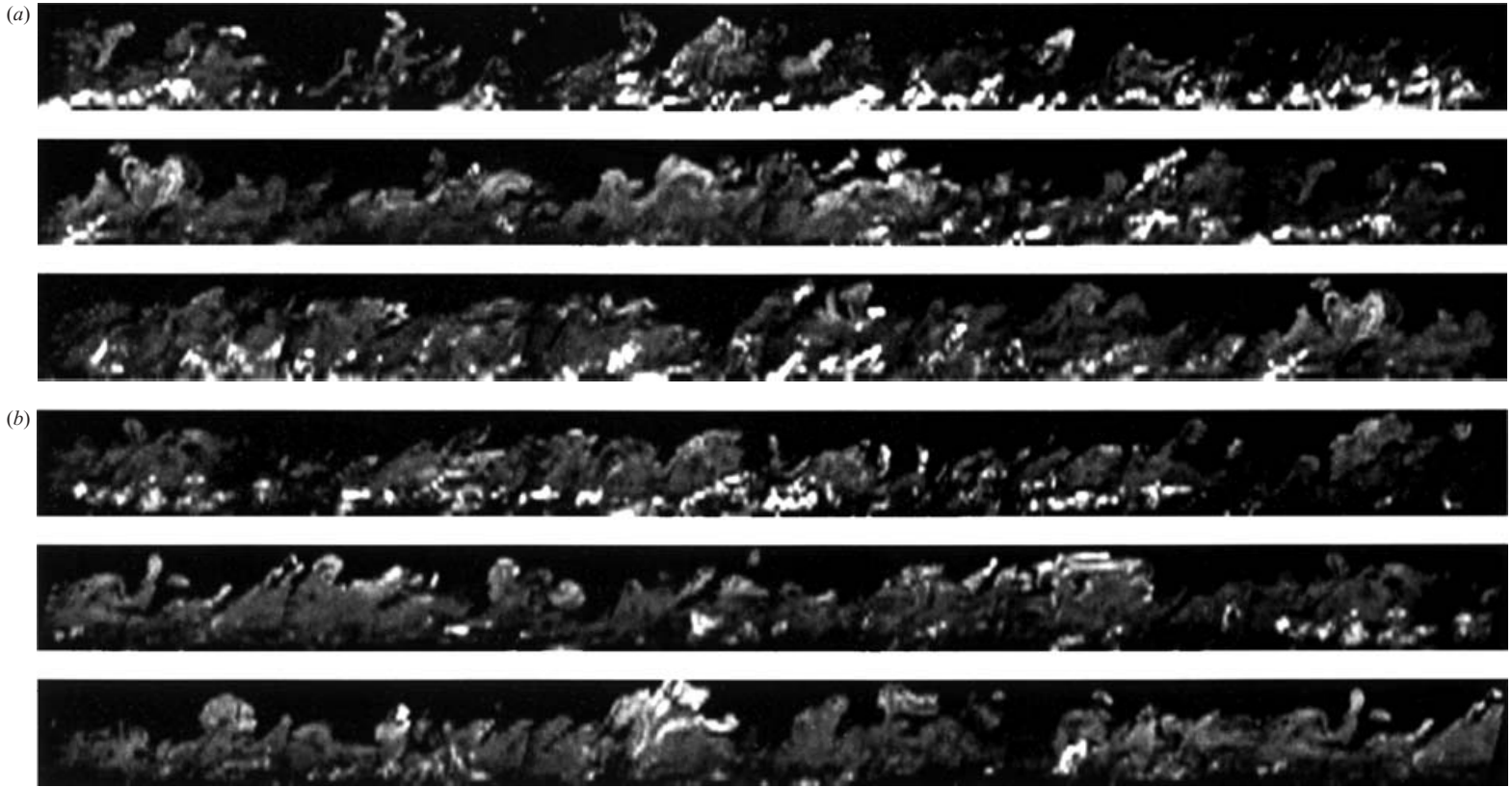
FIGURE 7. Resampled x–y images of the composite stack. 'Flow' is from left to right. Each of the two long strip images has been split into three segments, with portions repeated for clarity. Spanwise locations (a) $z^+ = 225$, (b) $z^+ = 425$. The streamwise and wall normal dimensions of each image are $L_x/\delta = 20.5$ by $L_y/\delta = 1.49$ ($L_x^+ = 6130$ by $L_y^+ = 440$).

coherent packets of near-wall fluid this far into the outer region of the boundary layer is remarkable (sometimes traversing a wall-normal distance of over 1δ while convecting downstream by a distance of only 1δ–2δ) and indicates significant momentum transfer. In particular, packets that have undergone such large wall-normal migrations generally appear to be physically connected to the upstream 'backs' of large outer-layer structures. This suggests that large scalar structures may grow through the engulfment of 'fresh' near-wall vortical fluid as they convect downstream. These observations are in strong agreement with the findings of Praturi & Brodkey (1978) and Nychas, Hershey & Brodkey (1973), for a turbulent boundary layer with a Reynolds number of 900, based on momentum thickness.

It is also important to note that the resliced x–y images, which are typical of visual investigations of turbulent boundary layers, tend to present a more complex picture of the boundary layer than actually exists. Considering the stereoscopic views of figure 6, it is apparent that, although complicated, the data set is populated by a relatively small number of large-scale vortical structures. This is consistent with the observation of Adrian *et al.* (2000) that, at low Reynolds numbers, packets (bulges) contain 2–3 hairpins. The resliced images, because they do not incorporate the spanwise dimension, sometimes cut a single contorted structure into several 'pieces' which may not appear to be connected. The slicing may also miss (in whole or in part) a large-scale structure directly adjacent to a bright streak due to a spanwise offset, hence underestimating or overlooking the possible influence of the structure on the motion of the near-wall fluid. The resulting picture of the boundary layer may overestimate the variety of structures present, or miss important aspects of the dynamics, particularly with respect to inner/outer-layer interactions that are distributed in the spanwise direction. The volumetric visualization technique was found to be essential in providing a clearer understanding of the complexity as well as the underlying order in the three-dimensional structure of the boundary layer.

4. Large-scale coherent structures

Several hundred stereoscopic views of the 50 volume data set were generated in order to qualitatively identify the large-scale coherent structures that were present, and to guide the subsequent quantitative analysis. For the initial examination, top and oblique views of the 50-volume time series were generated. A bottom view was used to identify bright streaks residing beneath large-scale structures, and to examine the motion of the streaks.

For the purpose of further discussion of specific scalar structures, three of the stereo visualizations from the top viewpoint are presented as stereopairs in figure 8. These represent time steps 1, 6 and 11 and are separated in time by 0.2 s ($\Delta t/t_\delta = \Delta T U_e/\delta = 1.70$, $\Delta t/\Delta t^+ = \Delta T u_\tau^2/\nu = 24.6$).

A total of 28 distinct large-scale outer-layer structures, labelled 'A–Ω', were identified from these and similar views from other time steps. The named structures are indicated in single projections of the volumes in figure 9, and are given in table 1, with general indications of the physical dimensions of each. These values were determined visually from the stereograms, and are therefore only crude approximations; however, mean values calculated from the chart ($\Delta \bar{x}/\delta = 1.3$ and $\Delta \bar{z}/\delta = 1.0$) lie within the range of values expected for the LSM. It is also important to note that many of the labelled structures are composed of multiple components. The grouping of components into single structures was done intuitively, to simplify the naming procedure, and does not necessarily imply that the structures were dynamically linked. Note also that not all
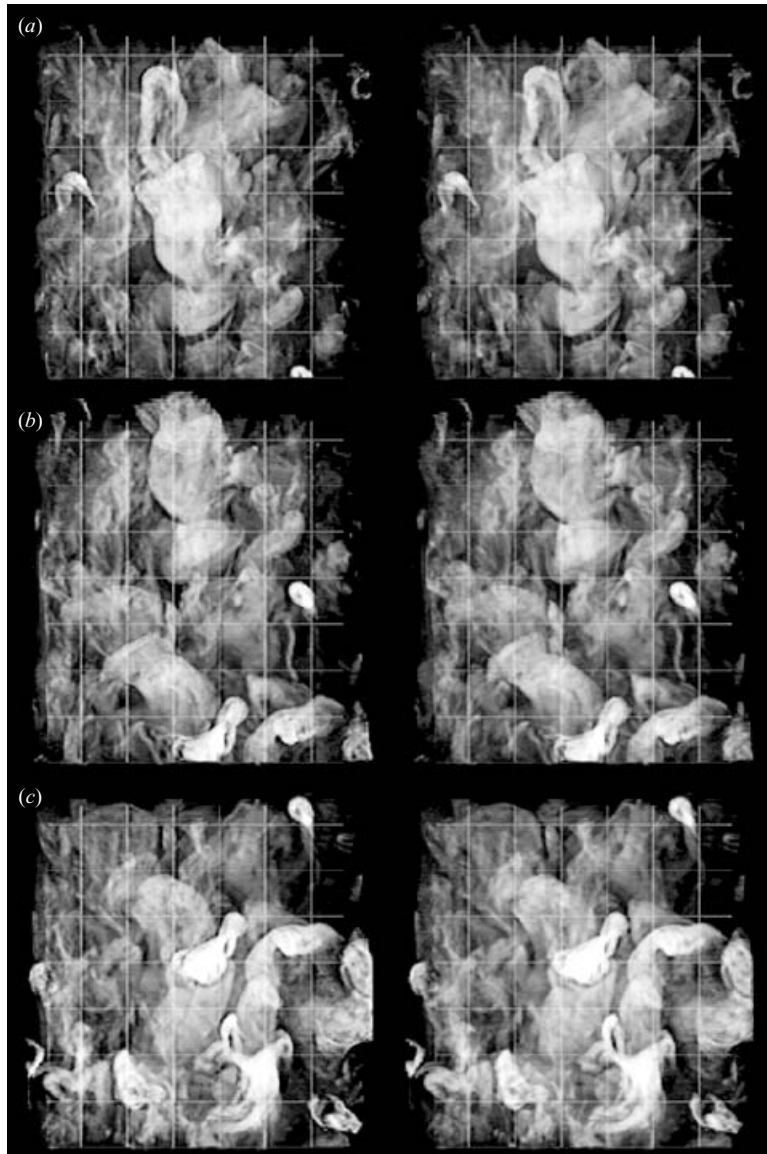
FIGURE 8. Stereoscopic visualization of (*a*) time step 1, (*b*) time step 6 and (*c*) time step 11, viewed from above the boundary layer. Flow is from the bottom of the page to the top, and the grid spacing is 0.5δ. The volumes span 3.53δ by 1.49δ by 3.34δ in the x-, y- and z-directions, respectively.

structures in the visualizations have been identified by name, so the named structures are a subjectively chosen subset of the whole.

The wide variety in shape and orientation of the large-scale structures is immediately apparent. There are a few structures with the general appearance of a horseshoe vortex (structures B, D, E, possibly O, and T). There is, however, no particular shape that can be considered to be dominant. The orientation of the structures with respect to the wall was found to be generally in accord with past observations; the structures
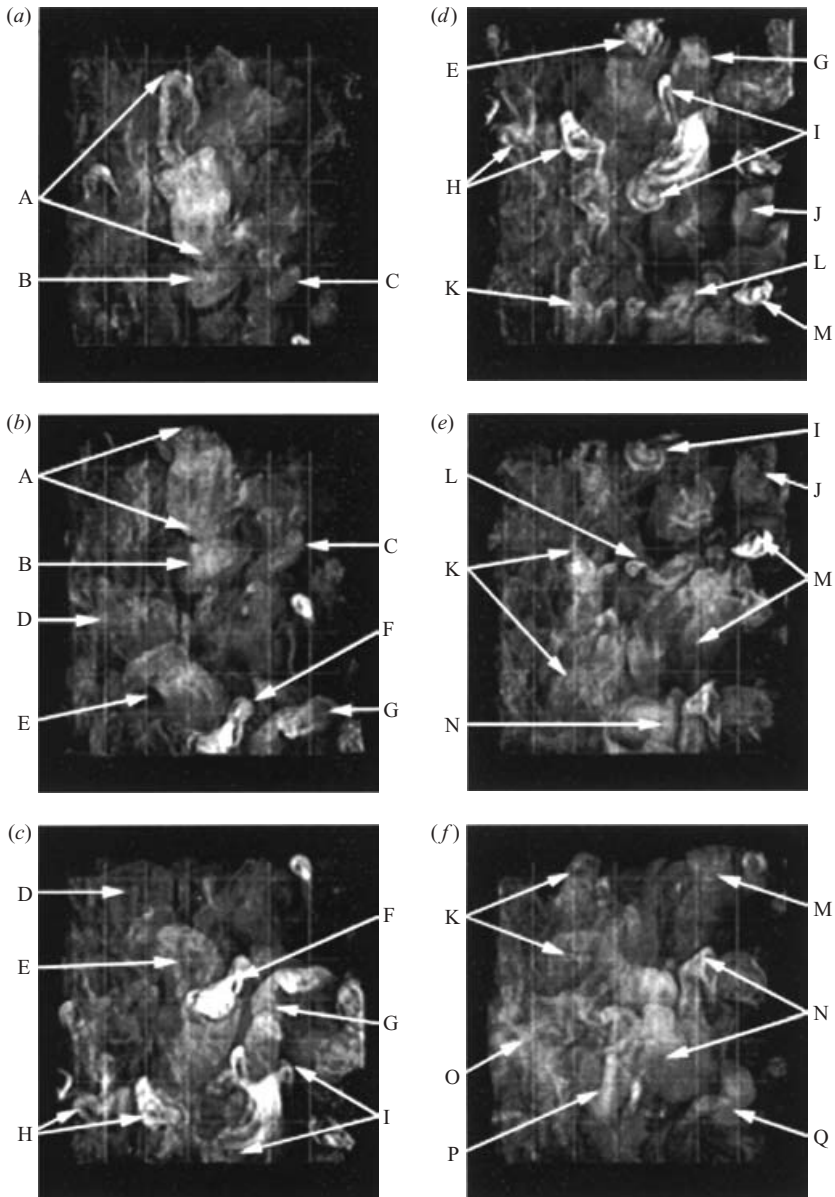
FIGURE 9(*a–f*). For caption see facing page.

generally lean in the downstream direction, with an inclination angle of approximately 45°, but with large variability.

The global spatial organization of the structures noted earlier in figures 4 and 6 is again apparent. The diagonal alignment is especially clear in the stereograms of time steps 11 (figure 8*c*), 36 and 41 (not shown). The structures appear to be regularly spaced along these diagonal lines, with a separation of approximately 1δ to 1.5δ. The diagonal spacing and the downstream inclination of the structures will be examined further later in this paper.
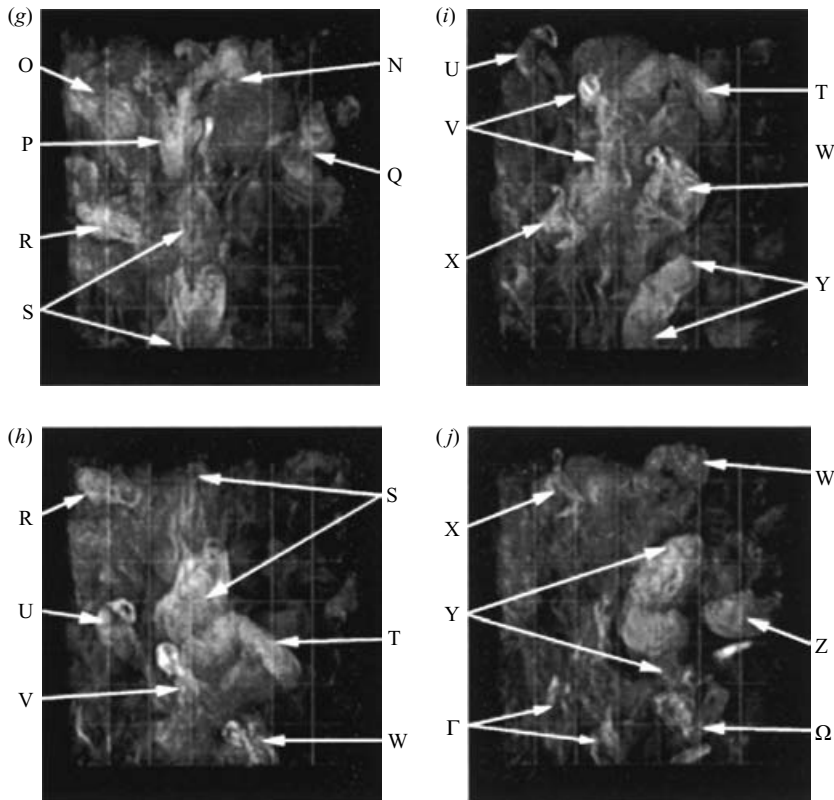
FIGURE 9. Naming convention for large-scale structures in the outer layer. (*a*) Time step 1; (*b*) 6; (*c*) 11; (*d*) 16; (*e*) 21; (*f*) 26; (*g*) 31; (*h*) 36; (*i*) 41; (*j*) 46. See also table 1.

The bright streaks in the inner layer were identified by lower case letters, related to the labelling of the large-scale structures, as shown in figure 10. The streak beneath structure D was labelled 'd', the single streak beneath structures A and B labelled 'a/b(1)', and so on. To determine the labelling, composite images of the 50 volume data set located at $y/\delta = 1.12$ and 0.297 were examined. The composite at $y/\delta = 1.12$ is the same as that presented in figure 4. The second composite, at $y/\delta = 0.297$, was assembled using the mean velocity at that height, in order to prevent 'double imaging' of the streaks due to their slower convection. The resulting inner-layer composite image is 15.4δ by 3.34δ in the *x*- and *z*-directions, respectively.

Note that the streak a/b(2) was not directly beneath an outer-layer structure, but was named in concert with the parallel streak a/b(1). In figure 10, some of the streaks appear to be made up of separate elements, but detailed examination of the data set and the stereoscopic visualizations suggested that they were portions of a single streak. Table 1 indicates which of the named large-scale structures appeared to be associated with near-wall streaks. All of the streaks identified in figure 10 were found to undergo lift-up, to varying degrees.

The relationship of the inner-layer streaks to outer-layer structure was examined using stereoscopic visualizations. The outer large-scale structures were made more transparent (see Delo 1996), allowing improved visualization of the wall streaks beneath them. Stereoscopic visualizations of time steps 8 and 39 prepared in this way

Name	Approximate size		Associated streak/lift-up	Comments
	Λ_x/δ	Λ_z/δ		
A	2.3	1.0	a/b(1), a/b(2)	Large, streamwise-aligned
B	0.6	0.9	a/b(1), a/b(2)	Possible horseshoe
C	0.8	0.7		Mushroom cross-section
D	0.9	1.4	d	Possible horseshoe
E	1.2	1.3	e/f	Possible horseshoe
F	1.6	1.0	e/f	Contorted, very bright
G	1.3	1.0		Contorted, very bright
H	0.8	1.4		Two-part, spanwise separation
I	1.7	1.1	i	Contorted, very bright
J	1.2	0.6		Compact
K	2.2	0.8	k	Large, streamwise-aligned
L	0.9	0.9	l/m	Compact
M	1.6	1.2	l/m	Large, diffuse
N	1.9	1.2		Large, diffuse
O	1.0	1.2	o	Possible horseshoe
P	1.5	0.6	p	Streamwise aligned loop
Q	1.0	1.0		Compact
R	1.2	1.3		Compact
S	2.2	1.0	s/v/y/ω	Large, streamwise-aligned
T	1.0	1.2		Possible horseshoe
U	1.0	0.8		Compact
V	1.3	0.8	s/v/y/ω	Slender, diffuse
W	1.3	0.9	w	Compact
X	1.0	0.8	x	Compact
Y	1.6	1.1	s/v/y/ω	Large, streamwise-aligned
Z	0.7	1.0		Two-part, streamwise separation
Λ	1.1	1.0	g	Two-part, spanwise separation
Ω	1.6	1.0	s/v/y/ω	Highly contorted, lobed

TABLE 1. Named large-scale coherent structures.

are shown in figures 11 and 12, respectively. Note the presence of the bright streaks directly beneath the structures A, B, D and E in time step 8 and beneath structures S, V, W and X in time step 39. The streaks have a sinuous shape, as would be expected in a low-speed wall streak undergoing unstable oscillations. Close examination of the stereograms of the subsequent time steps indicated that the streaks were lifting up, suggesting that they were associated with ejection events.

Examination of the oblique-view time series indicated that the lift-up of near-wall streaks sometimes occurred at several locations simultaneously across the data set. Oblique views of time steps 8 and 39 are also given in figures 11 and 12, again with the altered transparency function. Arrows in the figures indicate the portions of the streaks which appear to be undergoing simultaneous motions away from the wall. While not conclusive proof of ejections in themselves, the visualizations indicated that the presence of streaks underneath the large-scale structures was common (streaks were found beneath 18 of the 27 large-scale structures). Streak lift-up was also found to be common, and there were indications of spatial organization among the active streaks.

5. Correlation analysis of the large-scale structure

Correlation stacks were generated and examined in order to quantitatively characterize the large-scale structure in the 50 volume data set. In order to prevent
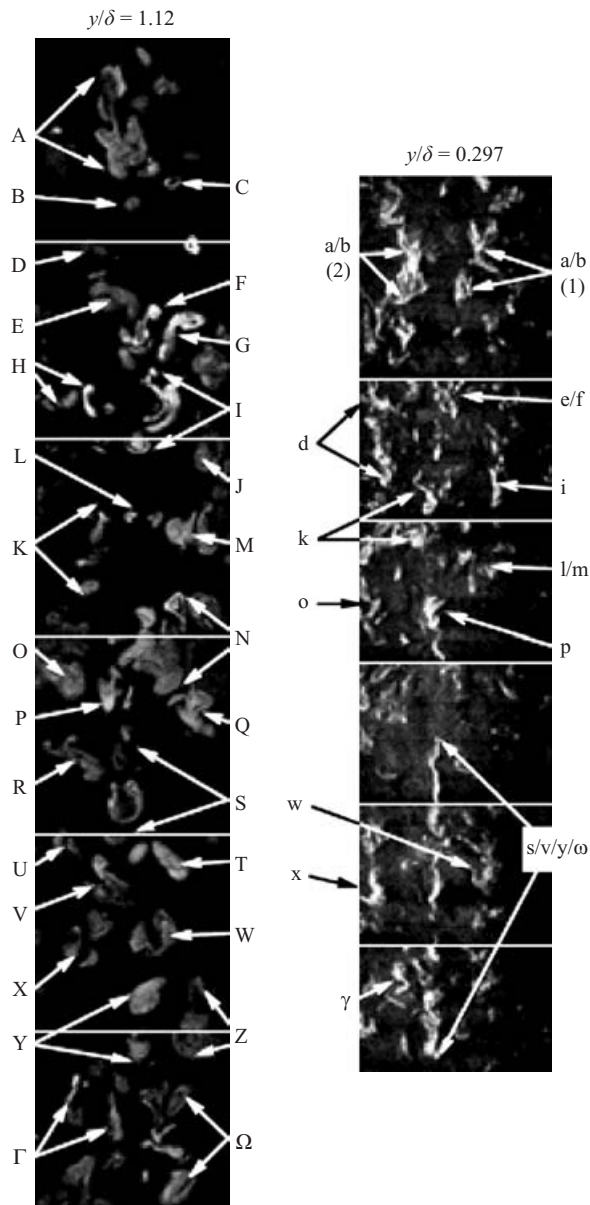
FIGURE 10. Naming convention for bright streaks in the inner layer. See also table 1. The top image is from time step 1; the next image is from time step 11, shifted vertically by $\Delta x = u\Delta t$, and so on, to time step 51. Cross-sections of the large-scale structures are identified as in figure 9.

biasing that might occur owing to repeated appearance of structures in subsequent volumes, the correlation stacks were derived from every tenth volume; time steps 6, 16, 26, 36 and 46 were used as base volumes for the correlation analysis. The volumes were separated in time by $3.41\,t_\delta$ or $49.3\,t^+$. In the outer layer, structures which convect near the free-stream velocity have moved almost completely through the volume, as can be seen by inspecting the single projections of figure 9.
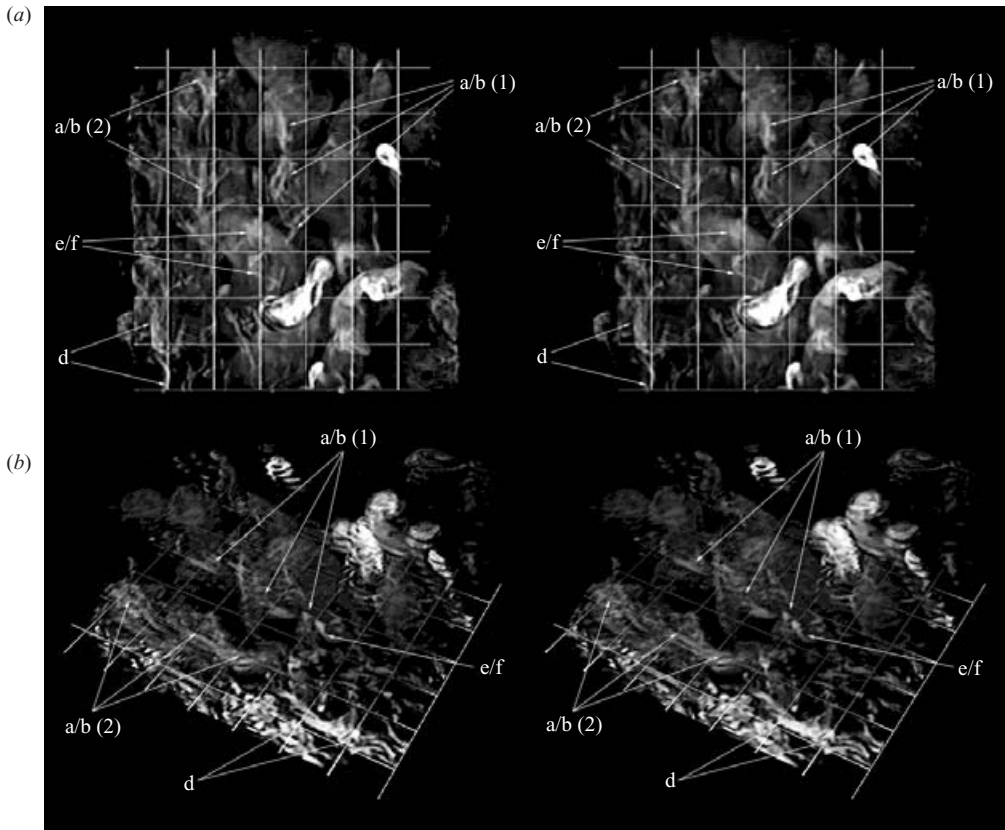
FIGURE 11. Stereoscopic visualization of time step 8, with transparency biased to reveal near-wall streaks. (*a*) Top view; (*b*) oblique view. Naming convention as in table 1.

In the near-wall region, convection velocities are lower, so it is expected that portions of the same bright streaks may appear in two subsequent base volumes. Examining the data slices in the near-wall region shows that the bright streaks are deforming at a high rate in both the spanwise and wall-normal directions. Space–time correlations were calculated to evaluate the convection and decay of the scalar structures (see below). It was found that the streaks had changed in character appreciably (as measured by the decrease in correlation coefficient) so that the auto-correlation stacks were not biased by the appearance of scalar structures in subsequent base volumes.

The base volume sets were compared on an individual basis, rather than by computing averages. The averaging process was attempted, but tended to disguise important structural features, and was of questionable value with the abbreviated data set.

5.1. *Autocorrelations*

Autocorrelation maps were computed for each of the 20 slices in the five base volumes, resulting in five autocorrelation stacks. Figure 13 shows the data from time step 6 which is representative of the other base volumes. Isocorrelation contours at four levels in the boundary layer have been added to the 'quantized' images (the 256 grey levels have been reduced to 12 grey scale bands corresponding to the correlation coefficient range −0.20 to 1.0 as shown in the calibration strip included with the image).
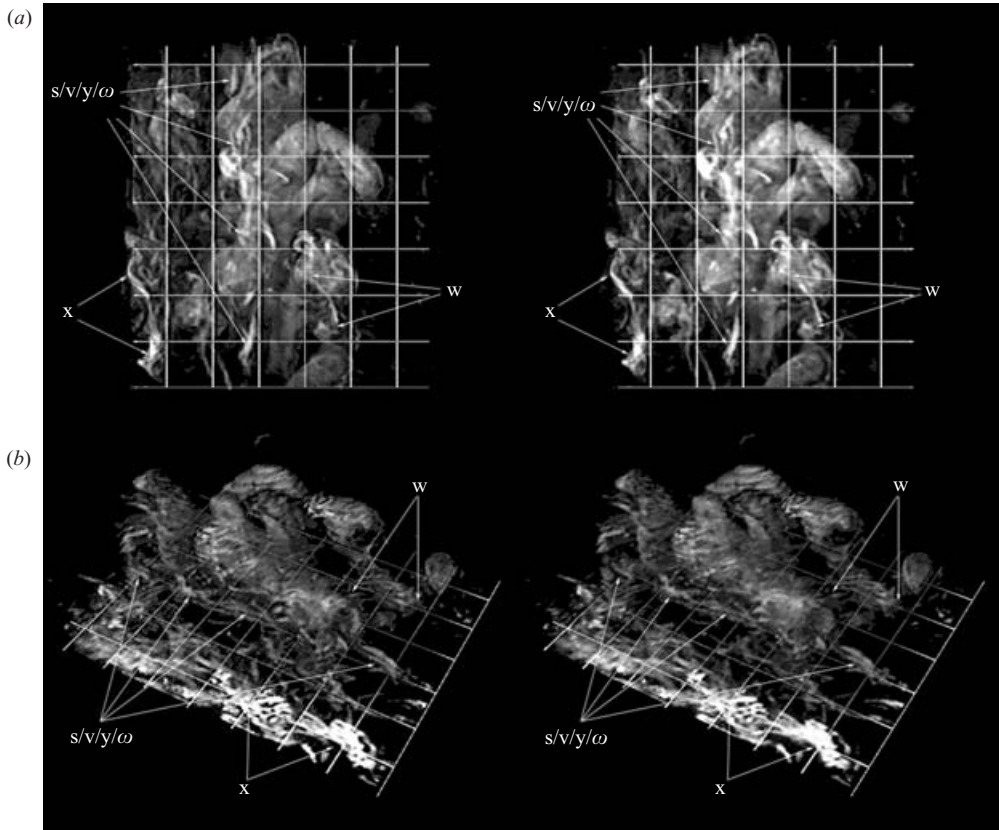
FIGURE 12. Stereoscopic visualization of time step 39, with transparency biased to reveal near-wall streaks. (*a*) Top view; (*b*) oblique view. Naming convention as in table 1.

The diagonal orientation of the large-scale structures in the (x, z)-plane is apparent to differing degrees in the autocorrelation maps. At the upper level shown, $y/\delta = 1.115$, diagonal lines drawn from the centre of the maps through off-centre local maxima fall in the range $\pm 50°$ from the x-axis. In most of the maps, more than one line of diagonal orientation was detectable. This is due to the spatial extent of the scalar images, each of which incorporates a large number of scalar structures. Each diagonal grouping of structures (with different orientations) makes a contribution to the correlation maps, resulting in the multiple local maxima. This diagonal orientation is reminiscent of the model of the turbulent spot proposed by Perry *et al.* [1981].

Time step 26 (see figure 9) was notably different from the others. The primary orientation at $y/\delta = 1.115$ was approximately 75° to the streamwise direction, and there were large spanwise bands of negative correlation which were not found in the other maps at this y-level. The stereoscopic visualization of time step 26 shows that this particular volume is quite complicated, with no obvious diagonal orientation of the structures in evidence. The negative correlation bands imply a two-dimensional periodicity in the streamwise direction, although this is difficult to detect in the stereogram.

The strong variation in the correlation maps at $y/\delta = 1.115$ in the boundary layer (which is even more marked in correlation maps at higher y-levels) suggests that
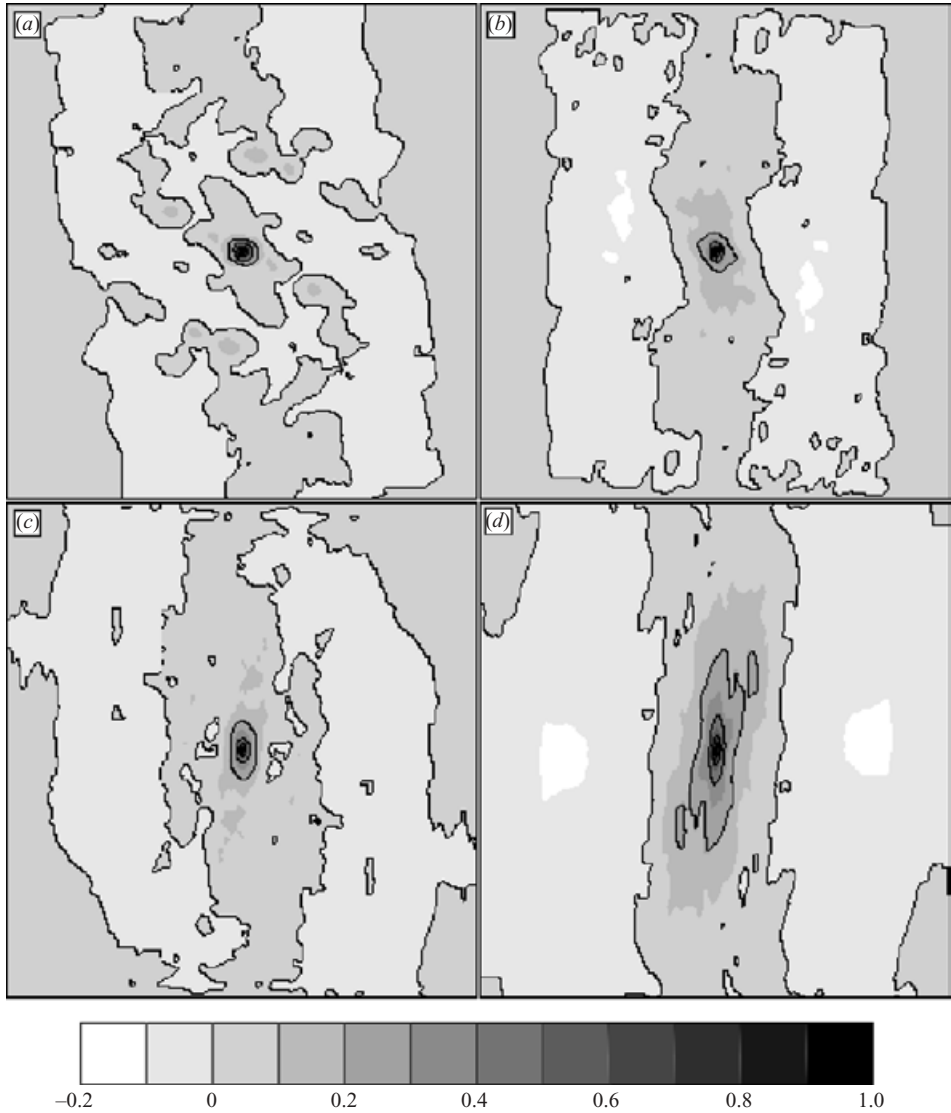
FIGURE 13. Autocorrelation maps in the (x, z)-plane generated from scalar data slices, time step 6. (a) $y/\delta = 1.115$; (b) $y/\delta = 0.743$; (c) $y/\delta = 0.372$; (d) $y/\delta = 0.074$. Isocorrelation contours indicated by grey scale level.

the data has not converged in the outer portion of the boundary layer, probably owing to the small statistical size of the data set. It also suggests that in an ensemble average of a large number of such correlation maps, the strong angular arrangement of structures within individual volumes might be smeared out. Although a statistically significant number of correlations in the outer layer were not calculated, the clear angular arrangement of large-scale structures in the outer part of the boundary layer has never before been as clearly revealed as it is here.

At the next lower y-level shown in figure 13, $y/\delta = 0.743$, the primary orientation of the structures falls within a much narrower range of approximately $\pm 10°$ to the x-direction, and the correlation maps from the base volumes are much more similar
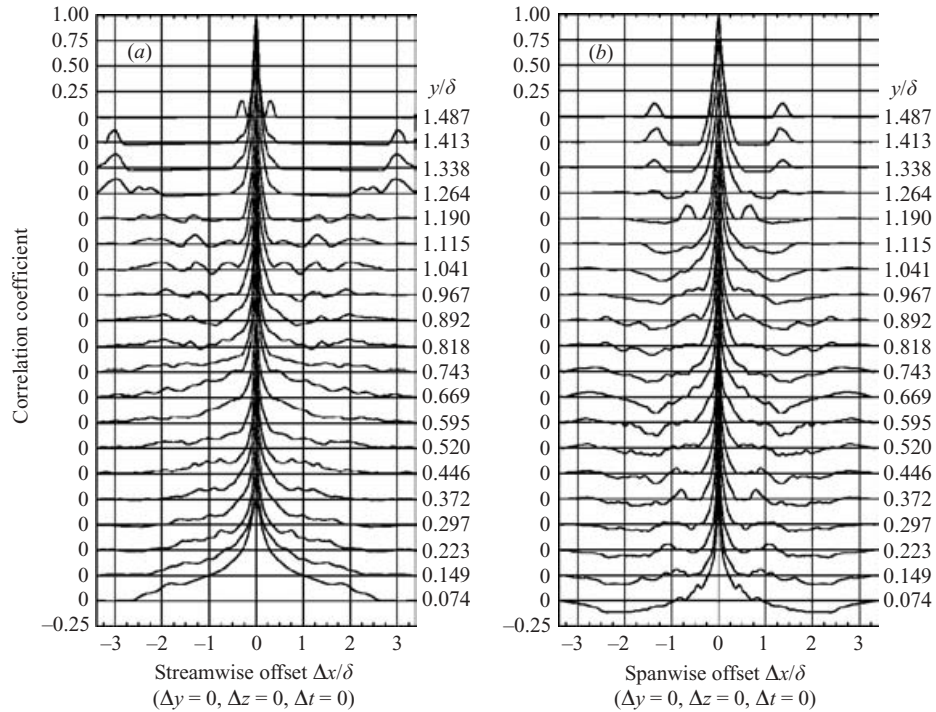
FIGURE 14. Autocorrelation coefficients for time step 6. (*a*) (*x*, *y*)-plane, along streamwise centreline; (*b*) (*y*, *z*)-plane, along spanwise centreline.

in nature. The range of orientation angles narrows as the wall is approached and, in the near-wall maps at $y/\delta = 0.074$, the orientation is very nearly streamwise. The maps themselves also become smoother and more similar at lower y-levels, indicating that the near-wall correlations have come closer to converging, probably due to the reduced range of structure size and shape and a statistically larger number of scalar structures found in the inner portion of the boundary layer.

The autocorrelation stacks (see figure 13) were resampled along the streamwise and spanwise centrelines (corresponding to zero spanwise and streamwise offset, respectively). The data were converted to both resampled images and plots of autocorrelation coefficient. The resampled x–y ($\Delta z = 0$) and y–z ($\Delta x = 0$) images showed evidence of a variation of structure size across the boundary layer (as inferred from isocontours), and evidence of streamwise and spanwise periodicity in some of the images. The plots of correlation coefficient as a function of y-level corresponding to the resampled images are given in figure 14. Here, the periodicity is shown by the appearance of secondary maxima at non-zero streamwise and spanwise offset. For example, in figure 14 there are secondary maxima at a streamwise separation $\approx 3\delta$ and spanwise separation $\approx 1.3\delta$ in the outer layer ($y/\delta \geqslant 1.2$). Spatial periodicity along other directions in the (x, z)-plane (not aligned with the x- or z-axes) will be discussed below.

The streamwise and spanwise length scales of the scalar structures at each of the 20 y-levels were determined from the x–z autocorrelation plots using the 0.2 isocontour as the threshold level. The variation in streamwise length scale (L_x,0.2) with y-level were averaged over the five base volumes and presented along with data from Smith (1994) in figure 15(*a*). The data from Smith are from isocontours of x–z correlation
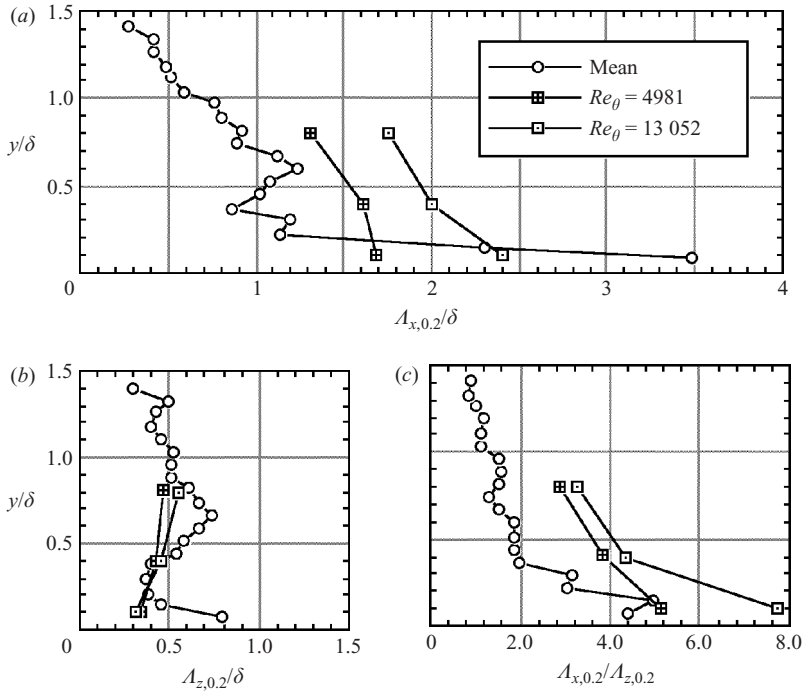
FIGURE 15. Mean length scales averaged over the five base volume data sets. (*a*) Streamwise direction; (*b*) spanwise direction; (*c*) ratio of streamwise to spanwise length scales. $\bigcirc$, new data, $Re_\theta = 700$; $\square$, $Re_\theta = 4981$ and $13\,052$, from Smith (1994).

maps based on cross-correlations of fluctuating streamwise velocity (u') recorded by two hot-wire probes separated in the spanwise direction.

In the present data, the mean streamwise length scale increases towards the wall, until $y/\delta \approx 0.6$. The scale decreases until the level $y/\delta \approx 0.4$ is reached, then increases again. The initial increase is in keeping with the data from Smith, as are the very long streamwise length scales found in the near-wall region. The data also suggest an increase in length scale with Reynolds number in the subsonic regime; however, the velocity correlations of Smith are fundamentally different from the scalar correlations performed here, so the apparent trend is inconclusive.

The decrease in the mean length scale in the middle portion of the boundary layer is somewhat puzzling, but is reflected in each of the individual plots and was assumed to be a real effect. From a detailed examination of both the original data slices and the resampled x–y time series (see below), packets of brightly dyed near-wall fluid were found in these levels of the boundary layer throughout the time span of the data set. By the time the packets had migrated from the near-wall region into the middle layers, the packets were generally compact in both the streamwise and spanwise directions. Since the correlations were computed on the basis of the grey scale values, the bright packets tend to dominate the correlation calculations. This provided a possible explanation for the decrease in streamwise length scale at these y-levels.

The mean spanwise length scales ($L\Lambda_{z,0.2}$) are shown in figure 15(*b*). The length scale is reasonably uniform in the outer part of the layer, but then increases. At $y/\delta \approx 0.7$ the scale decreases sharply, finally increasing again in the near-wall region. The

averaged plot is more complex than might have been expected from the limited data of Smith, but agreement is reasonable. In particular, there appears to be little effect of Reynolds number on the spanwise length scales in the velocity-based correlation data. The fact that the scalar correlations yield similar spanwise length scales is encouraging. The large increase in spanwise length scale at $y/\delta = 0.074$ in the scalar data is unexpected, and may be an additional artefact of over-dying the near-wall fluid.

Figure 15(*c*) shows the ratio of streamwise to spanwise length scales, or aspect ratio. The data indicate that near the outer edge of the layer ($y/\delta > 1$), structures have approximately unit aspect ratio; below this level, structures become highly elongated in the streamwise direction as the wall is approached, in general agreement with the data from numerous other investigations. Note that despite the decrease in the streamwise and spanwise length scales near $y/\delta \approx 0.4$, the aspect ratio of the structures shows a nearly uniform increase as the wall is approached.

5.2. *Space–time correlation*

To evaluate convection velocities for the scalar structures, space–time correlations were calculated at each of the 20 levels, for time delays of $1\Delta t$ to $8\Delta t$ ($\Delta t/t_\delta = 0.34$ to 2.72; $\Delta t^+ = 4.93$ to 39.4) and zero wall-normal separation ($\Delta y = 0$). For time step 46, only the time delays $1\Delta t$ to $4\Delta t$ were considered, as the primary data set extended only to time step 50. Individual x–z correlation images are not presented. For details, see Delo (1996).

Figure 16 shows the streamwise convection velocities of the scalar structures compared with the local mean velocity. In each case, there is a significant velocity deficit in the range $0.15 < y/\delta < 0.6$ ($45 < y^+ < 180$). There is also a deficit in the outer layer in the profile from time step 26. This may be evidence of a very large migration of low-speed fluid into the outer portion of the boundary layer. Such events will be examined in more detail in §6.

It is important to note that the free-stream and local mean velocities were obtained by correlating images of hydrogen bubbles, and the convection velocities of the dye-marked structures were obtained using the same correlation algorithm. Whereas the light scattered from the hydrogen bubbles is statistically similar at all locations in the flow, the light scattered and emitted from the dye is dependent on the local dye concentration. The correlations were computed on the basis of grey scale value, so the brightly dyed regions of the flow tend to dominate the correlations. Therefore, the measured 'convection velocities' will represent the velocities of the brightly marked regions.

The consistent velocity deficit in the lower half of the boundary layer shows that the brightly dyed fluid which dominates the near-wall images is moving more slowly than the local mean velocity. This implies that the dye injection method employed in the experiment does in fact mark the low-speed streaks in the near-wall region. The large wall-normal extent of the deficit is evidence that the low-speed fluid is ejected quite far from the wall, representing a significant exchange of momentum between the inner and outer layers.

As with the autocorrelation stacks, correlation coefficients were extracted from the streamwise centreline of the stacks and plotted, so that the decay in correlation coefficient with time could be examined. The results for time step 6 are shown in figure 17.

The resliced images and the correlation coefficients indicate that the most rapid decay of the scalar structures appears to be in the range $0.2 < y/\delta < 0.6$ ($60 < y^+ < 180$), which is also the range of large velocity deficit noted above. The
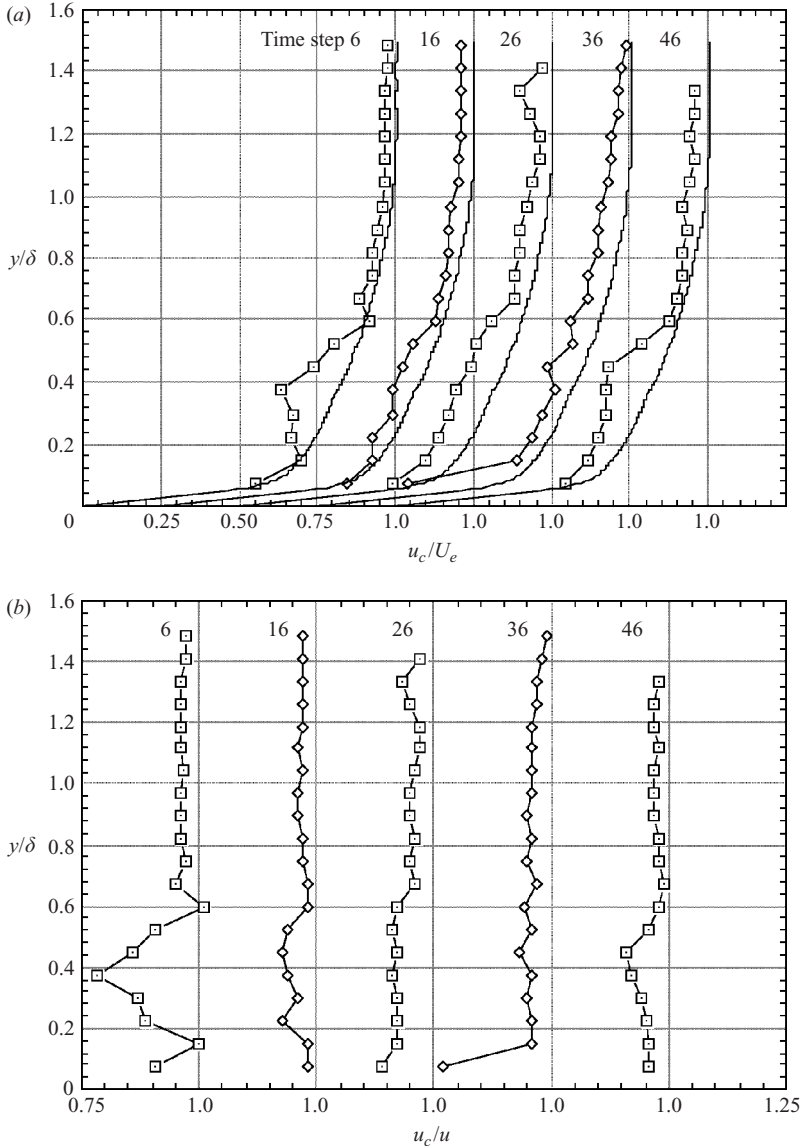
FIGURE 16. Mean convection velocities for the five basis volumes. (*a*) Profiles of u_c/U_e. The solid lines represent the mean velocity profile. (*b*) Profiles of u_c/u.

implication is that the scalar structures within this portion of the boundary layer are the most active. Several possibilities exist: the structures are either undergoing significant deformation as they convect downstream, or they traverse large spanwise and/or wall-normal distances in a relatively short time span, so that they move off the streamwise centreline (in the $\pm z$-direction) or out of the image plane (in the $\pm y$-direction). Individual x–z correlation maps did not reveal significant spanwise motion of the correlation peaks. Since the correlations are spatial averages, this implies that the mean spanwise motion of structures at a given height is approximately zero, with individual structures having an equal probability of moving in the positive or negative z-direction, verifying that the mean flow was two-dimensional.
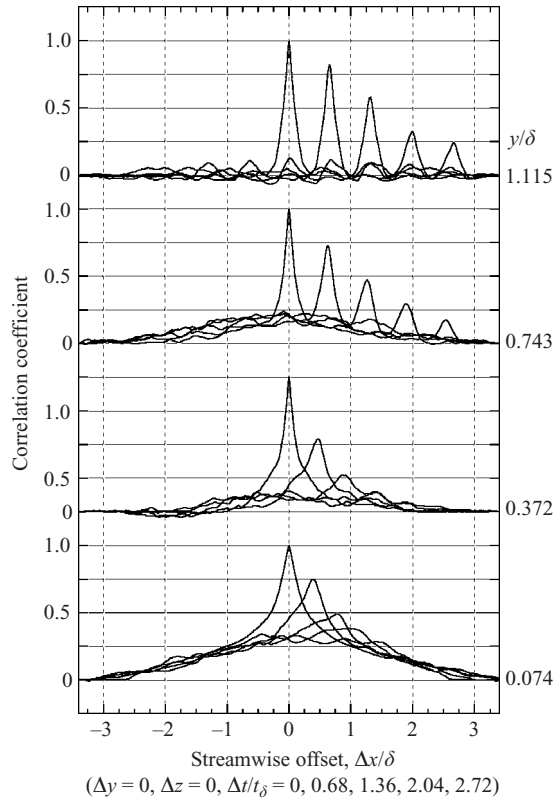
FIGURE 17. Decay of the correlation coefficient in the (x, y)-plane, time step 6, for $y/\delta = 1.115$, 0.743, 0.372 and 0.074, and time delays $\Delta t/t_d = 0.0$, 0.68, 1.36, 2.04 and 2.72.

As will be found in the next section, large-scale wall-normal migration of brightly dyed fluid packets from the near-wall region was detected throughout the data set. The rapid decay in the mid-levels of the boundary layer could be attributed to the passage of low-momentum fluid through the boundary layer in the positive y-direction, and its interaction with the less active scalar structures at that level. The appearance of fluid with significant momentum deficit at these levels may be causing the rapid distortion of what might otherwise be fairly inactive structures.

In the outer portion of the boundary layer, the slower decay is due to the largely inactive large-scale structures convecting downstream. At the two y-locations nearest the wall ($y/\delta = 0.149$ and 0.074) the slow decay is consistent with the long streamwise dimension and temporal persistence of the low-speed streaks. The issues mentioned earlier concerning the apparent convergence of the data in the near-wall region are also applicable.

To evaluate structure angles in the (x, y)-plane, correlations were computed between reference images at $y/\delta = 1.115$, 0.743 and 0.372 and the 19 other images in each base volume. These correlation stacks (three for each base volume) were resampled along the streamwise centreline, and x–y correlation maps with zero time delay were generated. For each of the three reference levels, the streamwise offset (Δx) of maximum correlation coefficient in the correlation stacks was found. The results in the vicinity of the reference level (approximately $\pm 0.25\delta$) showed the level of downstream inclination expected from the results of Smith (1994).
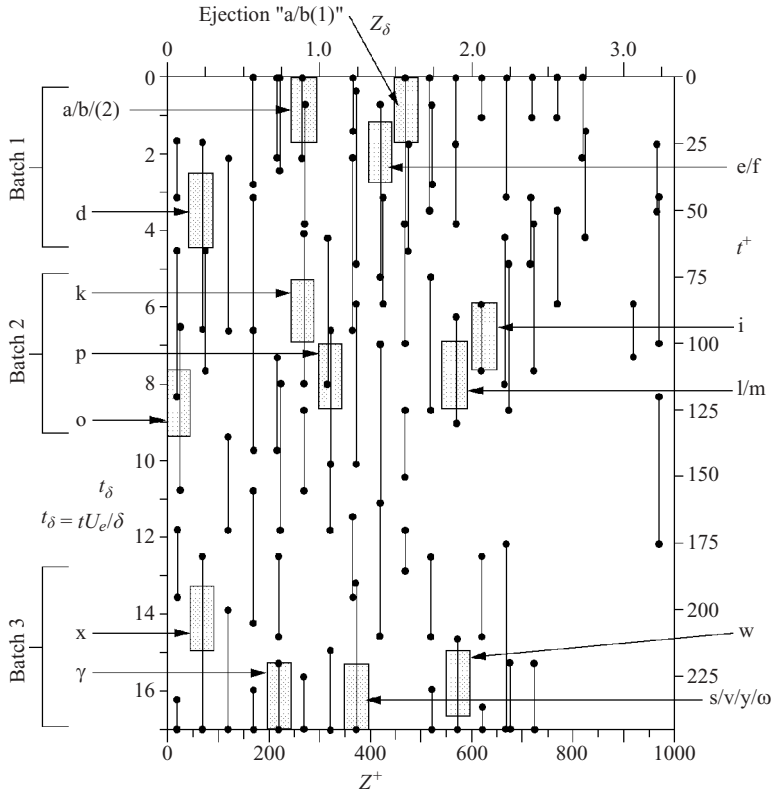
FIGURE 18. Ejection events identified from the resampled time series. Line segments represent portions of the time series in which discrete brightly dyed fluid 'packets' were observed to lift up. The boxes represent the thirteen ejection events identified and analysed.

As stated above, the spanwise locations of the maxima were also sampled. For a distance of about 0.3δ to 0.4δ ($\Delta z^+ = 90$ to 120) spanning the centre reference location, the offsets were close to zero. Closer to the wall, the offsets suddenly jumped to large negative values (Delo 1996), indicating a change in structure. This is suggestive of the spatial relationship to be expected from an idealized horseshoe vortex, with a streak located beneath a horseshoe vortex at a spanwise offset relative to the legs.

6. Near-wall dynamics

In order to examine the detailed behaviour of the near-wall streaks, 20 resampled time series were extracted from the data set. Each time series was composed of 50 x–y images (one from each time step), each of which was a spanwise average over 50 ℓ_{z^+} (0.17δ). The 20 averaged time series therefore covered the entire spanwise extent of the data set. The effect was to reslice the volumes into 20 equally spaced x–y slices.

Each of the time series was examined for evidence of brightly marked fluid moving away from the wall. The result of this examination is presented in figure 18. Line segments in the figure represent portions of the time series in which discrete brightly dyed fluid 'packets' were observed to cross constant y-level reference lines. The packets were identified visually. Overlapping lines at a given z-location indicate that distinct fluid packets were present at more than one streamwise location in a

given x–y image. A total of 75 individual line segments are included in the figure. However, line segments at adjacent z-locations may result from a lift-up having a large spanwise extent, or from significant spanwise motion during its evolution. Subsequent examination of the data slices indicated that this was the case. The 75 individual fluid packets were determined to be portions of 13 distinct bright near-wall streaks which were undergoing lift-up. The behaviour of each of the streaks was then examined to see if the motion of the bright fluid packets satisfied the criteria for an ejection.

To be considered an ejection, the bright fluid needed to demonstrate both a positive wall-normal velocity ($+v'$) and a streamwise velocity less than the local mean ($-u'$). All of the lift-ups that were examined satisfied the criteria at some point in time, and were considered to be evidence of the ejection of low momentum fluid into the outer portion of the boundary layer. To determine this, in each image, a horizontal (constant y-level) reference line was added to judge the wall-normal motion of the streak. Vertical reference lines (constant x-coordinate) were also added to the first image, in the vicinity of the bright fluid packets. The vertical reference lines were then deformed (similar to a time-line) in the later images, based on the mean velocity profile. In this way, the streamwise motion of the bright fluid (relative to the mean) could be determined.

The 13 separate lift-ups are considered below in time series of resampled x–y images. The lift-ups were of variable duration, as is apparent from figure 18; however, only six images from each lift-up sequence were displayed. The six images were extracted from the portion of the lift-up during which the fluid packets were undergoing the most rapid wall-normal motion, resulting in the violent ejection of near-wall fluid into the outer layer. The thirteen abbreviated time series depicting the ejection of low-speed fluid are shown relative to the original 75 candidate lift-ups in figure 18. This figure strongly implies that the violent ejection stage of the lift-up process was correlated in the spanwise direction, as suggested by the preliminary examination of the stereoscopic visualizations (that is, as shown by figures 11 and 12). Consequently, the ejections were grouped into three batches for the discussion which follows.

6.1. *Batch 1: streak lift-ups a/b(1), a/b(2), d and e/f*

These four lift-ups are found beneath the large-scale outer structure in the stereoscopic visualizations of time steps 1, 6 and 11 (figure 8), and of time step 8 (figure 11). The representative lift-up a/b (1) is shown in the resliced x–y time series in figure 19. All four lift-up sequences show the streaks deforming into a more or less sinuous shape in the (x, y)-plane, consisting of one or more 'arched' portions which undergo significant deformation. The top of the arch is the portion of the streak which is ejected from the inner layer. Occasionally, during its motion away from the wall, such an arched streak may appear to split into two or more separate bright filaments which are inclined in the downstream direction. Examination of the data slices invariably indicated that this was due to a simultaneous sinuous deformation in the (x, z)-plane. To some extent, this sinuous deformation in both the (x, y)- and (x, z)-planes was found during all the streak lift-ups.

For lift-up a/b(1), the time series covers time steps 1–6, and was centred at $z^+ = 475$, directly beneath the trailing edge of the structure A/B as indicated. Note the movement of the bright fluid through the upstream edge of the structure B, as would be expected from a near-wall low-speed streak interacting with a horseshoe vortex. It has already been noted that B had the general appearance of a horseshoe vortex, as determined from the stereoscopic visualizations. The motion of the near-wall fluid is consistent with the induced motion of an arched vortex loop.
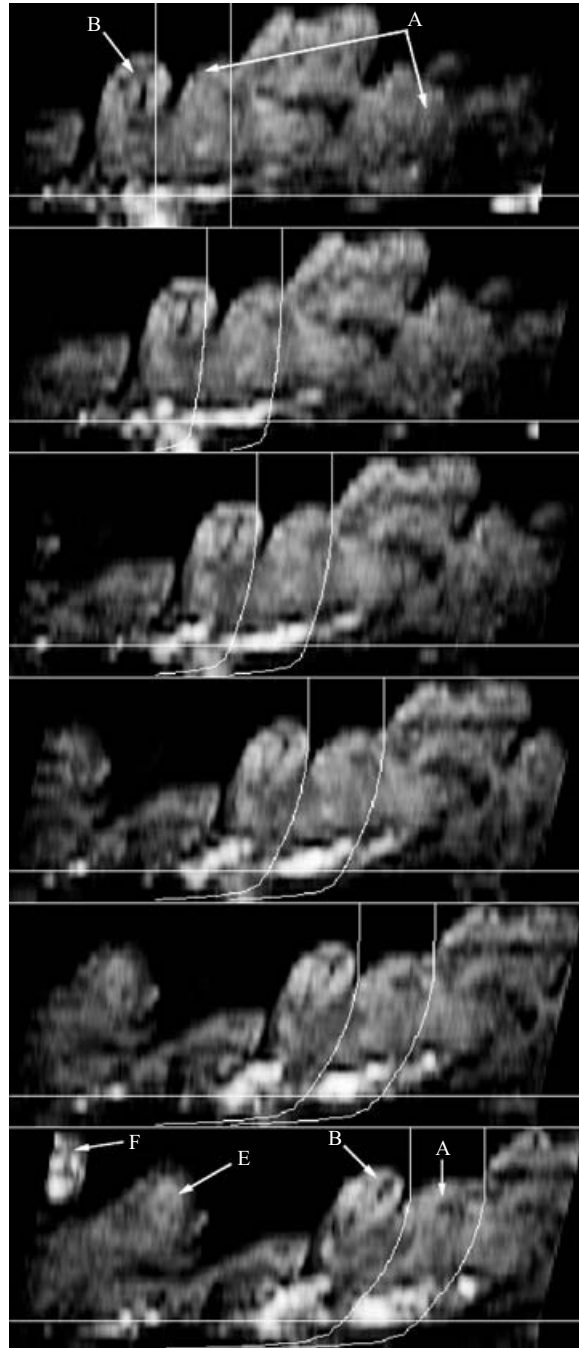
FIGURE 19. Streak lift-up '$a/b(1)$', as shown in resampled x–y images. Each image spans $L_x^+ = 1150$ (3.85δ) by $L_y^+ = 440$ (1.49δ), and was averaged over $50L_z^+$ (0.17δ), centred at $z^+ = 475$. The time series was extracted from time steps 1–6. Cross-sections of named structures are identified by letter. The vertical reference lines convect at the local mean velocity. The horizontal reference line is at $y/\delta = 0.20$. The bright fluid moves away from the wall ($+v'$) and slower than the local mean velocity ($-u'$) and was considered to be an ejection.

Also note the presence of the structure A directly preceding the horseshoe-like structure B. This quite large streamwise oriented structure appears to consolidate the streak a/b(1) beneath itself during its downstream progress. In this respect, it appears to 'organize' the streak prior to its interaction with the following compact horseshoe-like structure. Similar sequences of events are present in the other batches of ejections. The batch ejections tend to be preceded by a large ordered spanwise-diagonal collection of coherent structures.

During the lift-up a/b(2) (time steps 1–6, centred at $z^+ = 275$), the streak was not deformed as violently as in a/b(1). The initially arch-shaped streak was deformed in the streamwise direction, and appeared to fade during the time series. In this case, the bright fluid undergoes significant spanwise migration (in the $+z$-direction) during the series. This event is perhaps most notable because it did not appear to be associated with a large outer-layer structure. It is possible that a large-scale structure had moved through the volume just prior to the lift-up, but this was not investigated.

Lift-up d (time steps 8–13, centred at $z^+ = 75$) was a particularly large ejection of bright near-wall fluid, with a highly exaggerated arch shape, and it traversed a significant portion of the boundary layer. As with lift-up a/b(2), the lift-up was not preceded directly by a large-scale structure that can be seen. As the sequence is located at $z^+ = 75$ (near the edge of the volume), there is the additional possibility of a large-scale structure influencing the motion from just outside the field of view.

The compact bright fluid packets in the time series e/f (time steps 4–9, centred at $z^+ = 425$), were directly beneath the cross-section of the downstream-leaning structures E and F, closely following the large structures A and B. As previously noted, E had the general appearance of a horseshoe vortex. The movement away from the wall was not particularly marked, but there was a significant streamwise velocity deficit. Since the lift-up occurred nearly simultaneously and in close proximity to the lift-up a/b(1), it is probable that the ejections are initiated by the same trigger, namely the passage of the large agglomeration A/B.

6.2. *Batch 2: streak lift-ups i, k, l/m, o and p*

The ejections in this batch are similar in many respects to the first batch. The five lift-ups occurred nearly simultaneously, directly following the passage of the diagonal alignment of structures E/F/G/I, and occurred across the spanwise extent of the volume beneath the structures for which they are named.

A difference is exhibited by the ejection i (figure 20). Here, a large filament of brightly dyed fluid is being ejected well past the mean edge of the boundary layer. From examination of the source images and the stereoscopic visualizations of time steps 16 and 21, it is apparent that the filament, which is continuous into the near-wall region, is being strongly entrained into the trailing edge of structure I. The entrainment is highly three-dimensional and, in fact, the motion traverses approximately 0.5δ $(150\nu/u_\tau)$ in the z-direction while being ejected a corresponding distance in the y-direction. This ejection represents a very large momentum exchange across the boundary layer.

In the case of the lift-up k, the ejection occurred beneath the trailing edge of the structure K. This portion of the structure appeared to be a compact, possibly horseshoe-shaped, structure analogous to B, although it was not given a separate designation. In this respect, k was very similar to a/b(1), since the structure over the ejection is a long streamwise-oriented structure with a small horseshoe following it downstream. The sinuous deformation of the streak during this ejection was particularly marked.
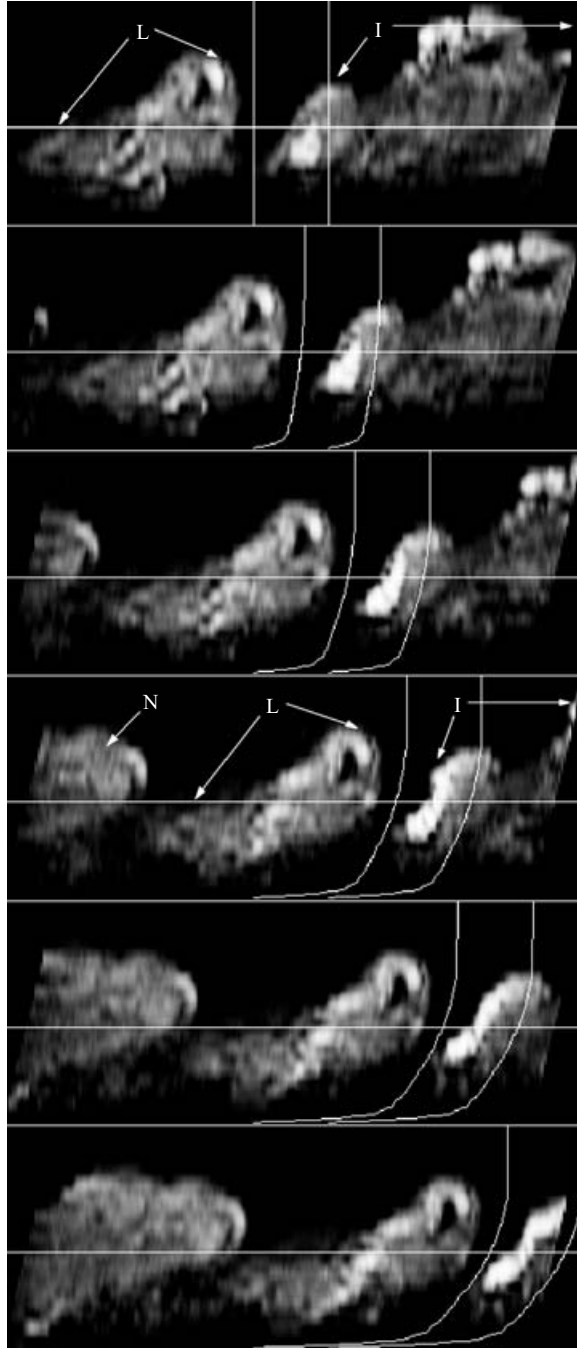
FIGURE 20. Streak lift-up 'i', as shown in resampled x–y images. Each image spans $L_x^+ = 1150$ (3.85δ) by $L_y^+ = 440$ (1.49δ), and was averaged over $50L_z^+$ (0.17δ), centred at $z^+ = 625$. The time series was extracted from time steps 18–23. Other details as for previous figure.

6.3. *Batch* 3: *streak lift-ups* $s/v/y/\omega$, w, x *and* γ

These are four nearly simultaneous ejections. There is a notable lack of activity (in terms of ejections) during time steps 28–39, as can be seen in the chart in figure 18.

In the outer portion of the boundary layer during this inactive time, there is a remarkable arrangement of structures. Two groups of structures, arranged at 45° to the streamwise direction, are clearly detectable in the stereoscopic visualizations. All the streaks which lift up are characterized by strong sinuous deformation. The passage of these two large diagonally oriented agglomerations of structures (R/S/T and U/V/W, figure 9) directly precedes the ejections in this batch and appears to organize the low-speed streaks prior to their interaction with the closely following structures X, Y and W.

The ejection s/v/y/w is very extensive in the streamwise direction, and is ejecting distinct fluid packets from at least three separate locations. As the streak is located beneath a continuous streamwise-oriented sequence of four large coherent structures, it is reasonable to suppose that these structures are, in fact, triggering the sinuous deformation of the streak and the subsequent ejections. The remaining ejections exhibit the characteristic sinuous deformation of the low-speed streaks prior to the ejection of the bright packets.

Considering the schematic plot of the ejection events as a function of time and spanwise location (figure 18), a very rough estimate can be made of a time delay for the batch bursting process; approximately 8 t_δ. From the experience of visually identifying the ejections, it seems unlikely that an automated routine would have been able to (i) identify the relatively small number of continuous streaks that were associated with the many lift-ups observed, and (ii) identify the final phase of the fluid ejection. From the highly variable spanwise location of the ejections and time delay between ejections at a given z-location, it is easy to see why the determination of bursting frequency has been the subject of much controversy. It would be useful to continue the detailed examination of subsequent time steps to determine whether the gaps between batches of ejections repeat at a discernible frequency. A statistically large sample of this type would also help to unravel the role of the large-scale agglomerations of coherent structures in the bursting process.

7. Discussion and conclusions

It is a difficult task to summarize the conclusions drawn from a project that has such a strong visual (i.e. subjective) component. A greater portion of the analysis reported here entailed the detailed examination of thousands of flow-visualization images, and the gradual development of a subjective understanding of the nature of the dynamic processes observed. The quantitative results that were derived from the volumetric scalar field were useful, and the comparison with previous quantitative boundary-layer studies was compelling. In particular, the length scales and angular orientation information derived from the correlation analysis of the scalar field showed encouraging agreement with the length scales reported by Smith (1994) in his detailed velocity-based investigation of the Reynolds-number effect on the structure of turbulent boundary layers.

The scalar structures observed in the volumetric data set are similar to those seen in numerous experimental investigations: two-dimensional cross-sections of the observed three-dimensional scalar structures, when compared to previous two-dimensional flow visualization studies, demonstrate this conclusively. In spite of the relatively small number of scalar structures observed, and the high degree of variability in their sizes and shapes, certain aspects of the structure and dynamics of the scalar field occurred with regularity, and were felt to be representative of low-Reynolds-number turbulent boundary layers and possibly turbulent boundary layers in general.

The apparent large-scale spanwise organization of individual scalar structures (streamwise and spanwise scale $\approx \delta$) along diagonal lines in the (x, z)-plane was very clear (this organization occurs throughout the complete 1600 volume data set). The lines were inclined to the free stream within the range $\pm 50°$. The spacing of the structures along the diagonal lines shows significant variability, but is approximately 1δ in the outer portion of the boundary layer. This spanwise organization of boundary-layer structure has not been documented extensively, although evidence supporting this observation may be found in previously published flow visualization studies.

Especially notable was the observation that groups of these large-scale scalar structures were frequently assembled into agglomerations measuring up to 5δ length. These very large scale streamwise and spanwise extensive agglomerations were oriented along diagonal lines within the same range noted above ($\pm 50°$). The agglomerations appeared to be spaced far apart in the streamwise direction ($\approx 8\delta$ to 10δ). Although relatively few of them were observed because of the large streamwise separation, this estimate was derived from long-time composites of the extended 151 volume data set (figure 6). The cross-stream extent of the data volume was not large enough to estimate their distribution in the spanwise direction.

The similar orientation of these very-large-scale agglomerations and the smaller-scale individual structures may provide clues to the formation of the agglomerations. It is possible evidence that the agglomerations have been formed through the merging of adjacent previously existing individual vortical structures as they convect downstream. However, fluctuating streamwise and spanwise velocities in the mid to outer levels of the boundary layer are insufficient to bring structures that are separated by $O(\delta)$ together within their lifetime, $O(6-10\,t_\delta)$. Also, vortex merging does not in itself explain the large-scale diagonal organization of the flow in the spanwise plane. It seems more likely that there are other phenomena at work, rather than simple vortex merging.

There is evidence that the large agglomerations grow through the addition of near-wall fluid as they convect downstream. Most of the ejection events identified in a spatial distribution occurred simultaneously, soon after the passage of the extended, large-scale structures. The fluid ejected by these events generally penetrated through the trailing edges of the structures, effectively increasing their streamwise extent. It is tentatively proposed that the addition of energetic near-wall fluid in this manner serves to perpetuate the active nature of the large-scale structures. The key seems to be the extended streamwise dimension of the large-scale agglomerations; these structures appear to be 'long' enough so that after perturbing the inner-layer low-speed streaks and triggering an ejection, the trailing edges of the structures are still in the neighbourhood to entrain the ejected near-wall fluid. Typically, after a streak lift-up and ejection, there is a quiescent period in which no ejections occur (figure 18), so no growth of the intermediate scalar structures would occur after the passage of such a large-scale structure. In this way, it may follow that the large-scale agglomerations grow preferentially, at the expense of smaller collections of structures.

The general diagonal orientation of the very large-scale agglomerations and the individual large-scale scalar structures in the outer portion of the boundary layer is similar in some respects to the underlying vortex field of a turbulent spot as proposed by Perry *et al.* (1981). In their model, an initial disturbance to a laminar boundary layer causes three-dimensional undulations in initially straight vortex bundles aligned in the spanwise direction. Fluctuating velocities induced by the wavy lines of vorticity cause the rapid growth of the turbulent spot in both the spanwise and streamwise directions, resulting in the patterns illustrated in Perry *et al.* (1981). It is probable

that there is a direct connection between the observed growth pattern of turbulent spots and the orientation observed in the turbulent boundary layer. This connection is especially interesting in light of the fact that the turbulent boundary layer in this study was tripped, so that the flow did not pass through the natural transition regime, during which turbulent spots arise spontaneously, grow and merge to fill the boundary layer. This suggests that the spanwise-diagonal organization may be the natural state of turbulent boundary layers, regardless of how they came into being. That the spanwise organization detected here is similar to the organization found both in turbulent spots and in turbulent boundary layers at much higher Reynolds number reinforces this conclusion.

Another aspect of the large-scale global organization of the flow was the observation that ejections of near-wall fluid appeared to be spatially organized and related to the passage of the large-scale agglomerations (figure 18). The motion of the thirteen observed near-wall streaks as they underwent oscillation, lift-up and ejection was roughly consistent throughout the data set and in line with previous models. During the ejection process, it was seen that a single streak can be associated with the ejection of more than one distinct fluid packet. Whether the packets should be considered separate ejections, or components of a single spatially distributed ejection is not clear.

An important observation was the sinuous spanwise deformation of the streaks during oscillation and lift-up, a clear indication of the three-dimensionality of the process. This was emphasized by the volumetric visualization of the dense population of scalar structures in the vicinity of the ejection events. It is evident that important influences on near-wall behaviour may be missed entirely by sampling the inherently three-dimensional boundary layer at a single point or in a single plane. Two-dimensional images, because they do not incorporate the third dimension, sometimes cut a single contorted structure into several 'pieces' which may not appear to be connected. The resulting picture of the boundary layer may overestimate the variety of structures present, or miss important aspects of the dynamics, particularly with respect to inner/outer-layer interactions that are distributed in the spanwise direction. For example, the slicing may miss (in whole or in part) a large-scale structure directly adjacent to a bright streak due to a spanwise offset, hence underestimating or neglecting the possible influence of the structure on the motion of the near-wall fluid. It is also evident that the inherently three-dimensional and spatially complex ejection process may not be well characterized by a single measure such as the bursting frequency. The highly contorted nature of the streaks, and the wide spatial distribution of the portions of the streak that were undergoing $-\overline{u'v'}$ motions, serve to explain some of the disparate results obtained by workers concerning the bursting process, particularly the bursting frequency (see, for example, Bogard & Tiederman 1986; Smith 1994).

Also important is the observation that near-wall fluid is sometimes ejected from the near-wall region well into the outer portion of the boundary layer ($y/\delta > 0.7$) while traversing a relatively short streamwise distance. This observation is in strong agreement with the three-dimensional observations of Praturi & Brodkey (1978). The arrival of fluid with high momentum deficit this far into the outer portion of the boundary layer represents significant momentum exchange. The fact that the near-wall fluid can penetrate this far over a relatively short time span implies that the outer portion of the boundary layer is quite active, and calls into question the view that outer-layer structures are simply the passive artefacts of events that happened far upstream, at least at the low-Reynolds-number regime investigated here. At higher Reynolds numbers, the greater separation in scales may serve to shelter the outer-layer

structure from the influence of the near-wall motions. However, the large-scale spatial organization and near-wall motions which were observed in this low-Reynolds-number investigation may still be present, although their influence may be confined to the logarithmic region in the boundary layer. Improved knowledge of the dynamics in the log layer would be very beneficial in itself, however, so the low-Reynolds-number results should not be dismissed as being too restricted to provide insights into turbulent boundary layers.

In conclusion, the volumetric approach adopted here for the study of the turbulent boundary layer was demonstrated to be well suited for the investigation of the complex three-dimensional time-dependent structures found in the flow. It should be pointed out that this project was limited to the detailed study of turbulent flow at a single Reynolds number. Hence, no explicit information was gained on the variation of structural features with Reynolds number. However, it is anticipated that the same type of global organization of turbulence can be expected in the near-wall-region of turbulent boundary layers at higher Reynolds number, although the scaling may differ in the details.

REFERENCES

ADRIAN, R. J., MEINHART, C. D. & TOMKINS, C. D. 2000 Vortex organization in the outer region of the turbulent boundary layer. *J. Fluid Mech.* **422**, 1–54.

BANDYOPADHYAY, P. R. 1980 Large structure with a characteristic upstream interface in turbulent boundary layers. *Phys. Fluids* **23**, 2326–2327.

BLACKWELDER, R. F. 1978 The bursting process in turbulent boundary layers. In *Coherent Structure of Turbulent Boundary Layers* (ed. C. R. Smith & D. E. Abbott). AFOSR/Lehigh University, Bethlehem, PA.

BLACKWELDER, R. F. & KAPLAN, R. E. 1976 On the wall structure of the turbulent boundary layer. *J. Fluid Mech.* **76**, 89–112.

BOGARD, D. G. & TIEDERMAN, W. G. 1986 Burst detection with single-point velocity measurements. *J. Fluid Mech.* **162**, 389–413.

BROWN, G. L. & THOMAS, A. S. W. 1977 Large structure in a turbulent boundary layer. *Phys. Fluids* **20**, S243–S252.

CANTWELL, B. J. 1981 Organized motion in turbulent flow. *Annu. Rev. Fluid Mech.* **13**, 457–515.

CHRISTENSEN, K. T. & ADRIAN, R. J. 2001 Statistical evidence of hairpin vortex packets in wall turbulence. *J. Fluid Mech.* **431**, 433–443.

DELO, C. 1996 Volumetric analysis of a low Reynolds number turbulent boundary layer. PhD thesis, Princeton University, Princeton NJ.

DELO, C., POGGIE, J. & SMITS, A. J. 1994 A system for imaging and displaying three-dimensional, time-evolving passive scalar concentration fields in fluid flow. TR 1992, Department of Mechanical and Aerospace Engineering, Princeton University.

DELO, C. & SMITS, A. J. 1993 Visualization of the three-dimensional, time-evolving scalar concentration field in a low Reynolds number turbulent boundary layer. In *Near-Wall Turbulent Flows* (ed. C. G. Speziale & B. E. Launder), pp. 573–582. Elsevier.

DELO, C. & SMITS, A. J. 1997 Volumetric visualization of coherent structure in a low Reynolds number turbulent boundary layer. *Intl J. Fluid Dyn.* **1**, art. 3 (URL http://elecpress.monash. edu.au/ijfd/1997_vol1/index.html).

ECKELMANN, H. 1974 The structure of the viscous sublayer and the adjacent wall region in a turbulent channel flow. *J. Fluid Mech.* **65**, 439–459.

GOLDSTEIN, J. E. 1991 Volumetric visualization of a low Reynolds number turbulent boundary layer. MSE thesis, Princeton University, Princeton, NJ.

GOLDSTEIN, J. E. & SMITS, A. J. 1994 Flow visualization of the three-dimensional, time-evolving structure of a turbulent boundary layer. *Phys. Fluids* **6**, 577–587.

HEAD, M. R. & BANDYOPADHYAY, P. R. 1981 New aspects of turbulent boundary layer structure. *J. Fluid Mech.* **107**, 297–338.

KIM, H. T., KLINE, S. J. & REYNOLDS, W. C. 1971 The production of turbulence near a smooth wall in a turbulent boundary layer. *J. Fluid Mech.* **50**, 133–160.

KLINE, S. J., REYNOLDS, W. C., SCHRAUB, F. A. & RUNSTADLER, P. W. 1967 The structure of turbulent boundary layers. *J. Fluid Mech.* **30**, 741–773.

KOVASZNAY, L. S. G., KIBENS, V. & BLACKWELDER, R. F. 1970 Large scale motion in the intermittent region of a turbulent boundary layer. *J. Fluid Mech.* **41**, 283–325.

LIU, Z., ADRIAN, R. J. & HANRATTY, T. J. 2001 Large-scale modes of turbulent channel flow: transport and structure. *J. Fluid Mech.* **448**, 53–80.

LU, L. J. & SMITH, C. R. 1985 Image processing of hydrogen bubble flow visualization for determination of turbulence statistics and bursting characteristics. *Exps. Fluids* **3**, 59–74.

LUCHIK, T. S. & TIEDERMAN, W. G. 1987 Timescale and structure of ejections and bursts in turbulent channel flows. *J. Fluid Mech.* **174**, 529–552.

MARUSIC, I. 2001 On the role of large-scale structures in wall turbulence. *Phys. Fluids* **13**, 735–743.

NYCHAS, G., HERSHEY, H. C. & BRODKEY, R. S. 1973 A visual study of turbulent shear flow. *J. Fluid Mech.* **61**, 513–540.

PERRY, A. E. & CHONG, M. S. 1982 On the mechanism of wall turbulence. *J. Fluid Mech.* **119**, pp. 173–219.

PERRY, A. E., LIM, T. T. & TEH, E. W. 1981 A visual study of turbulent spots. *J. Fluid Mech.* **104**, 387–405.

PRATURI, A. K. & BRODKEY, R. S. 1978 A stereoscopic visual study of coherent structure in turbulent shear flow. *J. Fluid Mech.* **89**, 251–272.

ROBINSON, S. K. 1991 Coherent motions in the turbulent boundary layer. *Annu. Rev. Fluid Mech.* **23**, 601–639.

SMITH, C. R. & SCHWARTZ, S. P. 1983 Observation of streamwise rotation in the near-wall region of a turbulent boundary layer. *Phys. Fluids* **26**, 641–652.

SMITH, C. R., WALKER, J. D. A., HAIDARI, A. H. & SOBRUN, U. 1991 On the dynamics of near-wall turbulence. *Phil. Trans. R. Soc. Lond.* A **336**, 131–175.

SMITH, M. W. & SMITS, A. J. 1995 Visualization of the structure of supersonic boundary layers. *Exps. Fluids* **18**, 288–302.

SMITH, R. W. 1994 Effect of Reynolds on the structure of turbulent boundary layers. PhD thesis, Princeton University, Princeton NJ.

ZHOU, J., ADRIAN, R. J., BALACHANDAR, S. & KENDALL, T. M. 1999 Mechanisms for generating coherent packets of hairpin vortices in channel flow. *J. Fluid Mech.* **387**, 353–396.